
Numerical results for mimetic discretization of Reissner-Mindlin plate problems

Lourenço Beirão da Veiga · Carlo Lovadina · David Mora

Abstract A low-order mimetic finite difference (MFD) method for Reissner-Mindlin plate problems is considered. Together with the source problem, the free vibration and the buckling problems are investigated. Full details about the scheme implementation are provided, and the numerical results on several different types of meshes are reported.

1 Introduction

The Reissner-Mindlin theory is widely used to describe the bending behavior of an elastic plate loaded by a transverse force. However, its discretization by means of Galerkin methods is typically not straightforward. For instance, standard low-order finite element schemes exhibit a severe lack of convergence whenever the thickness is too small with respect to the other characteristic dimensions of the plate. This undesirable phenomenon, known as *shear locking*, is nowadays well understood: as the plate thickness tends to zero, the Reissner-Mindlin model enforces the Kirchhoff constraint, which is typically too severe for the discrete scheme at hand, especially if low-order polynomials are employed (see, for instance, the monograph by Brezzi and Fortin [16]). The root of the shear locking phenomenon is that *the space of discrete functions which satisfy the Kirchhoff constraint is very small, and does not properly approximate a generic plate solution*. The most popular way to overcome the shear locking phenomenon in Galerkin methods is to reduce the influence of the shear energy

Lourenço Beirão da Veiga
Dipartimento di Matematica "F. Enriques", Università degli Studi di Milano,
Via Saldini 50, 20133 Milano, Italy
E-mail: lourenco.beirao@unimi.it

Carlo Lovadina
Dipartimento di Matematica, Università di Pavia,
Via Ferrata 1, I-27100 Pavia, Italy
E-mail: carlo.lovadina@unipv.it

David Mora
Departamento de Matemática, Universidad del Bío-Bío, Casilla 5-C, Concepción, Chile and
CI²MA, Universidad de Concepción, Concepción, Chile
E-mail: dmora@ubiobio.cl

by considering a (selective) reduced integration of the shear part, by resorting to a mixed formulation or by introducing a suitable *shear reduction operator*. Indeed, several families of methods have been rigorously shown to be free from locking and optimally convergent; let us mention, for instance, [1–4, 14, 17, 28, 29], and [37, 38, 40, 43, 44].

In the last years, many mimetic discretizations have been developed for the discretization of problems in partial differential equations. The mimetic finite difference (or MFD) method has been successfully employed for solving problems of electromagnetism [35], gas dynamics [21], linear diffusion (see, e.g., [8, 9, 12, 13, 15, 18, 19, 31, 32, 36] and the references therein), convection-diffusion [23], Stokes flow [6] and elasticity [5]. We also mention the development of a posteriori estimators for linear diffusion in [10] and post-processing technique in [22]. Finally, the mimetic discretization method has been shown to share strong similarities with the finite volume method in [26].

Recently, a mimetic finite difference (MFD) procedure has been proposed and theoretically analysed for Reissner-Mindlin plates in [11]. The method, which can be considered as a MFD version of the MITC and Durán-Liberman elements, combines the excellent convergence behaviour of the latter schemes with the great flexibility in handling the mesh of the former approach. The aim of this paper is to numerically assess the actual performance of the MFD method, by considering the source problem, as well as the free vibration and the plate buckling problems.

A brief outline of the paper is as follows. In Section 2 we recall the Reissner-Mindlin plate problems, together with the necessary notations. Section 3 concerns with a presentation of the numerical scheme proposed and analysed in [11]. In particular, full details about the method implementation, that were missing in [11], are provided. In Section 4 we report the numerical results obtained using several types of meshes. We end the paper with some concluding remarks.

2 The Reissner-Mindlin plate equations

Here and thereafter we use the following operator notation for any tensor field $\boldsymbol{\tau} = (\tau_{ij})$ $i, j = 1, 2$, any vector field $\boldsymbol{\eta} = (\eta_i)$ $i = 1, 2$ and any scalar field v :

$$\begin{aligned} \operatorname{div} \boldsymbol{\eta} &:= \partial_1 \eta_1 + \partial_2 \eta_2, & \operatorname{rot} \boldsymbol{\eta} &:= \partial_1 \eta_2 - \partial_2 \eta_1, & \operatorname{tr}(\boldsymbol{\tau}) &:= \tau_{11} + \tau_{22}, \\ \nabla v &:= \begin{pmatrix} \partial_1 v \\ \partial_2 v \end{pmatrix}, & \operatorname{curl} v &:= \begin{pmatrix} \partial_2 v \\ -\partial_1 v \end{pmatrix}, & \mathbf{div} \boldsymbol{\tau} &:= \begin{pmatrix} \partial_1 \tau_{11} + \partial_2 \tau_{12} \\ \partial_1 \tau_{21} + \partial_2 \tau_{22} \end{pmatrix}. \end{aligned}$$

Consider an elastic plate of thickness t such that $0 < t \leq \operatorname{diam}(\Omega)$, with reference configuration $\Omega \times (-\frac{t}{2}, \frac{t}{2})$, where Ω is a convex polygonal domain of \mathbb{R}^2 occupied by the midsection of the plate. The deformation of the plate is described by means of the Reissner-Mindlin model in terms of the rotations $\boldsymbol{\beta} = (\beta_1, \beta_2)$ of the fibers initially normal to the plate's midsurface, the scaled shear stresses $\boldsymbol{\gamma} = (\gamma_1, \gamma_2)$, and the transverse displacement w . Assuming that the plate is clamped on its whole boundary $\partial\Omega$, the following strong equations describe the plate's response to conveniently scaled transversal load $g \in L^2(\Omega)$: find $(\boldsymbol{\beta}, w, \boldsymbol{\gamma})$ such that

$$\begin{cases} -\operatorname{div} \mathbb{C}\boldsymbol{\varepsilon}(\boldsymbol{\beta}) - \boldsymbol{\gamma} = \mathbf{0} & \text{in } \Omega, \\ -\operatorname{div} \boldsymbol{\gamma} = g & \text{in } \Omega, \\ \boldsymbol{\gamma} = \kappa t^{-2}(\nabla w - \boldsymbol{\beta}) & \text{in } \Omega, \\ \boldsymbol{\beta} = \mathbf{0}, w = 0 & \text{on } \partial\Omega, \end{cases} \quad (1)$$

where the tensor of bending moduli is given by:

$$\mathbb{C}\boldsymbol{\tau} := \frac{\mathbb{E}}{12(1-\nu^2)} ((1-\nu)\boldsymbol{\tau} + \nu\text{tr}(\boldsymbol{\tau})\mathbf{I}),$$

with $\mathbb{E} > 0$ representing the Young modulus, $0 < \nu < 1/2$ being the Poisson ratio for the material and \mathbf{I} indicating the second order identity tensor.

Let the $H_0^1(\Omega)^2$ -elliptic bilinear form be given by

$$a(\boldsymbol{\beta}, \boldsymbol{\eta}) := \int_{\Omega} \mathbb{C}\boldsymbol{\varepsilon}(\boldsymbol{\beta}) : \boldsymbol{\varepsilon}(\boldsymbol{\eta}) = \frac{\mathbb{E}}{12(1-\nu^2)} \int_{\Omega} [(1-\nu)\boldsymbol{\varepsilon}(\boldsymbol{\beta}) : \boldsymbol{\varepsilon}(\boldsymbol{\eta}) + \nu \text{div } \boldsymbol{\beta} \text{ div } \boldsymbol{\eta}], \quad (2)$$

with $\boldsymbol{\varepsilon} = (\varepsilon_{ij})_{1 \leq i, j \leq 2}$ the standard strain tensor defined by $\varepsilon_{ij}(\boldsymbol{\beta}) := \frac{1}{2}(\partial_i \beta_j + \partial_j \beta_i)$, $1 \leq i, j \leq 2$.

Then, the variational formulation of problem (1) reads:

Problem 1 Find $(\boldsymbol{\beta}, w) \in H_0^1(\Omega)^2 \times H_0^1(\Omega)$ such that

$$a(\boldsymbol{\beta}, \boldsymbol{\eta}) + \kappa t^{-2} (\nabla w - \boldsymbol{\beta}, \nabla v - \boldsymbol{\eta})_{0, \Omega} = (g, v)_{0, \Omega} \quad \forall (\boldsymbol{\eta}, v) \in H_0^1(\Omega)^2 \times H_0^1(\Omega).$$

In this expression, $\kappa := \mathbb{E}k/2(1+\nu)$ is the shear modulus with k a correction factor usually taken as $5/6$ for clamped plates.

We will also consider the free vibration and buckling problem for plates.

The free vibration problem of a plate is (see [25, 27, 28, 30]):

Problem 2 Find $\lambda \in \mathbb{R}$ and $0 \neq (\boldsymbol{\beta}, w) \in H_0^1(\Omega)^2 \times H_0^1(\Omega)$ such that

$$a(\boldsymbol{\beta}, \boldsymbol{\eta}) + \kappa t^{-2} (\nabla w - \boldsymbol{\beta}, \nabla v - \boldsymbol{\eta})_{0, \Omega} = \lambda \left[(w, v)_{0, \Omega} + \frac{t^2}{12} (\boldsymbol{\beta}, \boldsymbol{\eta})_{0, \Omega} \right]$$

for all $(\boldsymbol{\eta}, v) \in H_0^1(\Omega)^2 \times H_0^1(\Omega)$, where $\lambda = \rho\omega^2/t^2$, with ρ being the density and ω the angular vibration frequency of the plate and the corresponding eigenfunctions are the vibration modes.

The buckling problem of a plate is (see [33, 39]):

Problem 3 Find $\lambda^{bp} \in \mathbb{R}$ and $0 \neq (\boldsymbol{\beta}, w) \in H_0^1(\Omega)^2 \times H_0^1(\Omega)$ such that

$$a(\boldsymbol{\beta}, \boldsymbol{\eta}) + \kappa t^{-2} (\nabla w - \boldsymbol{\beta}, \nabla v - \boldsymbol{\eta})_{0, \Omega} = \lambda^{bp} (\boldsymbol{\sigma} \nabla w, \nabla v)_{0, \Omega} \quad \forall (\boldsymbol{\eta}, v) \in H_0^1(\Omega)^2 \times H_0^1(\Omega),$$

where $\boldsymbol{\sigma}(x, y) \in \mathbb{R}^{2 \times 2}$ is a symmetric tensor which corresponds to a pre-existing stress state in the plate, $\lambda^{bp} = \lambda^{bc}/t^2$, with λ^{bc} being the buckling coefficients of the plate and the corresponding eigenfunctions are the buckling modes.

Accordingly with (1), for the problems above the scaled shear stresses can be computed by $\boldsymbol{\gamma} = \kappa t^{-2} (\nabla w - \boldsymbol{\beta})$.

3 A Mimetic Finite Difference (MFD) discretization

In this section we review the mimetic discretization method for the Reissner-Mindlin plate bending problem presented in [11], and extend it to the free vibration and buckling problems. Finally, in Section 3.6 we give the details on the implementation of the method.

3.1 Notation and assumptions

Let $\{\mathcal{T}_h\}_h$ be a sequence of decompositions of the computational domain Ω into $\mathcal{N}(\mathcal{T}_h)$ polygons E . We assume that this partition is conformal, i.e. intersection of two different elements E_1 and E_2 is either a few mesh vertices, or a few mesh edges (two adjacent elements may share more than one edge) or empty. We allow \mathcal{T}_h to contain non-convex and degenerate elements. For each polygon E , $|E|$ denotes its area, h_E denotes its diameter and $h := \max_{E \in \mathcal{T}_h} h_E$.

We denote the set of mesh vertices and edges by \mathcal{V}_h and \mathcal{E}_h , the set of internal vertices and edges by \mathcal{V}_h^0 and \mathcal{E}_h^0 , the set of vertices and edges of a particular element E by \mathcal{V}_h^E and \mathcal{E}_h^E , and the set of boundary vertices and edges by \mathcal{V}_h^∂ and \mathcal{E}_h^∂ , respectively. Moreover, we denote a generic mesh vertex by \mathbf{v} , a generic edge by \mathbf{e} and its length both by $h_{\mathbf{e}}$ and $|\mathbf{e}|$.

A fixed orientation is also set for the mesh \mathcal{T}_h , which is reflected by a unit normal vector $\mathbf{n}_{\mathbf{e}}$, $\mathbf{e} \in \mathcal{E}_h$, fixed once for all. Moreover, $\mathbf{t}_{\mathbf{e}}$ denotes the tangent vector defined as the counterclockwise rotation of $\mathbf{n}_{\mathbf{e}}$ by $\pi/2$.

For every polygon E and edge $\mathbf{e} \in \mathcal{E}_h^E$, we define a unit normal vector $\mathbf{n}_E^{\mathbf{e}}$ that points outside of E , and by $\mathbf{t}_E^{\mathbf{e}}$ the tangent vector as the counterclockwise rotation of $\mathbf{n}_E^{\mathbf{e}}$ by $\pi/2$.

The mesh is assumed to satisfy the shape regularity properties detailed in [11].

We make also the following assumption on the data. The scalar functions \mathbb{E}, ν are piecewise constant with respect to the mesh \mathcal{T}_h . Moreover, there exist two positive constants C_\star and C^\star such that $C_\star < \mathbb{E} < C^\star$ on the whole domain. The above uniformity condition on \mathbb{E} is standard, while the piecewise constant condition can be interpreted as an approximation of the data and is introduced only for simplicity. In the general case, it is sufficient to assume that \mathbb{E} and ν are (piecewise) $W^{1,\infty}$ and to introduce an element-wise averaging in the data of the numerical scheme.

3.2 Degrees of freedom and interpolation operators

The discretization of Problems 1-3 requires to discretize the scalar field of displacement and the vector fields of rotations and shears. In order to do so, we introduce the degrees of freedom for the numerical solution in accordance with the correspondence

$$\begin{aligned} w, v \in H_0^1(\Omega) &\rightarrow w_h, v_h \in W_h, \\ \boldsymbol{\beta}, \boldsymbol{\eta} \in H_0^1(\Omega)^2 &\rightarrow \boldsymbol{\beta}_h, \boldsymbol{\eta}_h \in H_h, \\ \boldsymbol{\gamma}, \boldsymbol{\delta} \in L^2(\Omega)^2 &\rightarrow \boldsymbol{\gamma}_h, \boldsymbol{\delta}_h \in \Gamma_h, \end{aligned}$$

where W_h represents the linear space of discrete displacement, H_h indicates the linear space of discrete rotations and Γ_h is the linear space of discrete shears.

The discrete space for transverse displacements W_h is defined as follows: a vector $v_h \in W_h$ consists of a collection of degrees of freedom

$$v_h := \{v^{\mathbf{v}}\}_{\mathbf{v} \in \mathcal{V}_h^0},$$

one per internal mesh vertex, e.g. to every vertex $\mathbf{v} \in \mathcal{V}_h^0$, we associate a real number $v^{\mathbf{v}}$. The scalar $v^{\mathbf{v}}$ represents the nodal value of the underlying discrete scalar field of displacement. The number of unknowns is equal to the number of internal vertices.

The discrete space for rotations H_h is defined as follows: a vector $\boldsymbol{\eta}_h \in H_h$ is a collection of degrees of freedom

$$\boldsymbol{\eta}_h = \{\boldsymbol{\eta}^{\mathbf{v}}\}_{\mathbf{v} \in \mathcal{V}_h^0},$$

i.e. we assign a vector $\boldsymbol{\eta}^{\mathbf{v}} \in \mathbb{R}^2$ per each vertex $\mathbf{v} \in \mathcal{V}_h^0$. The vector $\boldsymbol{\eta}^{\mathbf{v}}$ represents the nodal values of the underlying discrete vector field of rotations. The number of unknowns is equal to twice the number of internal vertices.

Finally, the space for the discrete shear force Γ_h is defined as follows: to every element $E \in \mathcal{T}_h$ and every edge $\mathbf{e} \in \mathcal{E}_h^E \cap \mathcal{E}_h^0$, we associate a number $\delta_E^{\mathbf{e}}$, i.e.

$$\boldsymbol{\delta}_h = \{\delta_E^{\mathbf{e}}\}_{E \in \mathcal{T}_h, \mathbf{e} \in \mathcal{E}_h^E \cap \mathcal{E}_h^0}.$$

We make the continuity assumption that for each edge \mathbf{e} shared by two element E_1 and E_2 , we have

$$\delta_{E_1}^{\mathbf{e}} = -\delta_{E_2}^{\mathbf{e}}.$$

The scalar $\delta_E^{\mathbf{e}}$ represents the average on edges of the discrete shears in the tangential direction. The number of unknowns is equal to the number of internal edges.

We now define the following interpolation operators from the spaces of smooth enough functions to the discrete spaces W_h , H_h and Γ_h , respectively. For every function $v \in C^0(\Omega) \cap H_0^1(\Omega)$, we define $v_{\mathbf{I}} \in W_h$ by

$$v_{\mathbf{I}}^{\mathbf{v}} := v(\mathbf{v}) \quad \forall \mathbf{v} \in \mathcal{V}_h^0. \quad (3)$$

For every function $\boldsymbol{\eta} \in [C^0(\Omega) \cap H_0^1(\Omega)]^2$, we define $\boldsymbol{\eta}_{\mathbf{I}} \in H_h$ by

$$\boldsymbol{\eta}_{\mathbf{I}}^{\mathbf{v}} := \boldsymbol{\eta}(\mathbf{v}) \quad \forall \mathbf{v} \in \mathcal{V}_h^0. \quad (4)$$

For every function $\boldsymbol{\delta} \in H_0(\text{rot}; \Omega) \cap L^s(\Omega)^2$, $s > 2$, we define $\boldsymbol{\delta}_{\text{II}} \in \Gamma_h$ by

$$(\delta_{\text{II}})_{\mathbf{e}}^{\mathbf{e}} := \frac{1}{|\mathbf{e}|} \int_{\mathbf{e}} \boldsymbol{\delta} \cdot \mathbf{t}_{\mathbf{e}} \quad \forall E \in \mathcal{T}_h \quad \forall \mathbf{e} \in \mathcal{E}_h^E \cap \mathcal{E}_h^0. \quad (5)$$

For all $E \in \mathcal{T}_h$ in the sequel we will also make use of local interpolation operators $v_{\mathbf{I},E}$, $\boldsymbol{\eta}_{\mathbf{I},E}$, $\boldsymbol{\delta}_{\text{II},E}$, with values in $W_h|_E$, $H_h|_E$, $\Gamma_h|_E$ respectively; such operators are simply the obvious restriction of the global ones to the element E for functions which are sufficiently regular on E .

Remark 1 We note that in the present paper we are considering the scheme of [11] without the edge bubbles, see Remark 4 of [11]. Such version of the method is more efficient in terms of accuracy vs number of degrees of freedom, while the loss of stability is seen only on very particular mesh patterns. Indeed, in the numerical test of Section 4, only the first family of (triangular) meshes suffers from such drawback.

3.3 Discrete norms and operators

We endow the space W_h with the following norm

$$\|v_h\|_{W_h}^2 := \sum_{E \in \mathcal{T}_h} \|v_h\|_{W_h, E}^2 = \sum_{E \in \mathcal{T}_h} |E| \sum_{\mathbf{e} \in \mathcal{E}_h^E} \left[\frac{1}{|\mathbf{e}|} (v^{\mathbf{v}_2} - v^{\mathbf{v}_1}) \right]^2, \quad (6)$$

where \mathbf{v}_1 and \mathbf{v}_2 are the vertices of \mathbf{e} . Although irrelevant in (6), in the following we will always consider that \mathbf{v}_1 and \mathbf{v}_2 , the vertices of a generic edge \mathbf{e} , are oriented in such a way that $\mathbf{t}_E^{\mathbf{e}}$ points from \mathbf{v}_1 to \mathbf{v}_2 .

In the space H_h , we consider the norm

$$\|\boldsymbol{\eta}_h\|_{H_h}^2 := \sum_{E \in \mathcal{T}_h} \|\boldsymbol{\eta}_h\|_{H_h, E}^2 = \sum_{E \in \mathcal{T}_h} |E| \sum_{\mathbf{e} \in \mathcal{E}_h^E} \left[\frac{1}{|\mathbf{e}|} \|\boldsymbol{\eta}^{\mathbf{v}_1} - \boldsymbol{\eta}^{\mathbf{v}_2}\| \right]^2, \quad (7)$$

where \mathbf{v}_1 and \mathbf{v}_2 are the vertices of the edge \mathbf{e} , and $\|\cdot\|$ denotes the euclidean norm on vectors.

In the space Γ_h , we consider the following norm

$$\|\delta_h\|_{\Gamma_h}^2 := \sum_{E \in \mathcal{T}_h} \|\delta_h\|_{\Gamma_h, E}^2 = \sum_{E \in \mathcal{T}_h} |E| \sum_{\mathbf{e} \in \mathcal{E}_h^E} |\delta_E^{\mathbf{e}}|^2. \quad (8)$$

The norms on W_h and H_h are $H^1(\Omega)$ type discrete semi-norms, which become norms due to the boundary conditions on the spaces, while the norm for Γ_h is an $L^2(\Omega)$ type discrete norm.

In the sequel we will also use the following norm on H_h , which is a $\|\boldsymbol{\varepsilon}(\cdot)\|_{0, \Omega}$ type discrete norm:

$$\|\boldsymbol{\eta}_h\|_{H_h}^2 := \sum_{E \in \mathcal{T}_h} \|\boldsymbol{\eta}_h\|_{H_h, E}^2 = \sum_{E \in \mathcal{T}_h} \min_{\mathbf{c} \in \mathbb{R}} \|\boldsymbol{\eta}_h - \mathbf{c}([-\bar{y}, \bar{x}])_{\mathbf{I}, E}\|_{H_h, E}^2, \quad (9)$$

where (\bar{x}, \bar{y}) are local cartesian coordinates on E which are null on the barycenter of E , so that the function $[-\bar{y}, \bar{x}]$ represents a (linearized) rotation around the barycenter.

We now introduce the discrete gradient operator ∇_h , defined from the set of nodal unknowns W_h to the set of edge unknowns Γ_h as follows:

$$\nabla_h : W_h \rightarrow \Gamma_h$$

$$(\nabla_h v_h)_E^{\mathbf{e}} := \frac{1}{|\mathbf{e}|} (v^{\mathbf{v}_2} - v^{\mathbf{v}_1}) \quad \forall E \in \mathcal{T}_h, \quad \forall \mathbf{e} \in \mathcal{E}_h^E \cap \mathcal{E}_h^0, \quad \forall v_h \in W_h,$$

where \mathbf{v}_1 and \mathbf{v}_2 are the vertices of \mathbf{e} .

We consider also a reduction operator, defined from the discrete space of rotations H_h to the set of edge unknowns Γ_h as follows:

$$\Pi_h : H_h \rightarrow \Gamma_h$$

$$(\Pi_h \boldsymbol{\eta}_h)_E^{\mathbf{e}} := \frac{1}{2} [\boldsymbol{\eta}^{\mathbf{v}_1} + \boldsymbol{\eta}^{\mathbf{v}_2}] \cdot \mathbf{t}_E^{\mathbf{e}} \quad \forall E \in \mathcal{T}_h, \quad \forall \mathbf{e} \in \mathcal{E}_h^E, \quad \forall \boldsymbol{\eta}_h \in H_h,$$

where \mathbf{v}_1 and \mathbf{v}_2 are the vertices of \mathbf{e} .

3.4 Scalar products and bilinear forms

We equip the space Γ_h with a suitable scalar product, defined as follows:

$$[\boldsymbol{\gamma}_h, \boldsymbol{\delta}_h]_{\Gamma_h} := \sum_{E \in \mathcal{T}_h} [\boldsymbol{\gamma}_h, \boldsymbol{\delta}_h]_{\Gamma_h, E}, \quad (10)$$

where $[\cdot, \cdot]_{\Gamma_h, E}$ is a discrete scalar product on the element E .

The scalar product must satisfy the following stability and consistency conditions (see [11]).

(S1) There exist two positive constants c_1 and c_2 independent of h such that, for every $\boldsymbol{\delta}_h \in \Gamma_h$ and each $E \in \mathcal{T}_h$, we have

$$c_1 \|\boldsymbol{\delta}_h\|_{\Gamma_h, E}^2 \leq [\boldsymbol{\delta}_h, \boldsymbol{\delta}_h]_{\Gamma_h, E} \leq c_2 \|\boldsymbol{\delta}_h\|_{\Gamma_h, E}^2. \quad (11)$$

(S2) For every element E , every scalar linear function p_1 on E and every $\boldsymbol{\delta}_h \in \Gamma_h$, we have

$$[(\mathbf{curl} p_1)_{\Pi}, \boldsymbol{\delta}_h]_{\Gamma_h, E} = \int_E p_1 (\mathbf{rot}_{\Gamma_h} \boldsymbol{\delta}_h)_E - \sum_{\mathbf{e} \in \mathcal{E}_h^E} \delta_E^{\mathbf{e}} \int_{\mathbf{e}} p_1, \quad (12)$$

where the operator $(\mathbf{rot}_{\Gamma_h} \boldsymbol{\delta}_h)_E := \frac{1}{|E|} \sum_{\mathbf{e} \in \mathcal{E}_h^E} \delta_E^{\mathbf{e}} |\mathbf{e}|$.

We denote with $a_h(\cdot, \cdot) : H_h \times H_h \rightarrow \mathbb{R}$ the discretization of the bilinear form $a(\cdot, \cdot)$, defined as follows (see (2)):

$$a_h(\boldsymbol{\beta}_h, \boldsymbol{\eta}_h) = \sum_{E \in \mathcal{T}_h} a_h^E(\boldsymbol{\beta}_h, \boldsymbol{\eta}_h) \quad \forall \boldsymbol{\beta}_h, \boldsymbol{\eta}_h \in H_h, \quad (13)$$

where $a_h^E(\cdot, \cdot)$ is a symmetric bilinear form on each element E , mimicking

$$a_h^E(\boldsymbol{\beta}_h, \boldsymbol{\eta}_h) \sim \int_E \mathbb{C}\boldsymbol{\varepsilon}(\tilde{\boldsymbol{\beta}}_h) : \boldsymbol{\varepsilon}(\tilde{\boldsymbol{\eta}}_h).$$

Similarly to the previous case, we introduce a stability and consistency assumptions for the local bilinear form $a_h^E(\cdot, \cdot)$.

(S1_a) there exist two positive constants \tilde{c}_1 and \tilde{c}_2 independent of h such that, for every $\boldsymbol{\eta}_h \in H_h$ and each $E \in \mathcal{T}_h$, we have

$$\tilde{c}_1 \|\boldsymbol{\eta}_h\|_{H_h, E}^2 \leq a_h^E(\boldsymbol{\eta}_h, \boldsymbol{\eta}_h) \leq \tilde{c}_2 \|\boldsymbol{\eta}_h\|_{H_h, E}^2. \quad (14)$$

(S2_a) For every element E , every linear vector function \mathbf{p}_1 on E , and every $\boldsymbol{\eta}_h \in H_h$, it holds

$$a_h^E((\mathbf{p}_1)_{\mathbf{I}}, \boldsymbol{\eta}_h) = \sum_{\mathbf{e} \in \mathcal{E}_h^E} \left[(\mathbb{C}\boldsymbol{\varepsilon}(\mathbf{p}_1) \mathbf{n}_E^{\mathbf{e}}) \cdot \left(\frac{|\mathbf{e}|}{2} [\boldsymbol{\eta}^{\mathbf{v}^1} + \boldsymbol{\eta}^{\mathbf{v}^2}] \right) \right]. \quad (15)$$

Remark 2 The scalar product and the bilinear form shown in this section can be built element by element in a simple algebraic way. The details are shown in Section 3.6.

3.5 The discrete method

Finally, we are able to define the mimetic discrete method for Reissner-Mindlin plates proposed in [11]. Let the loading term

$$(g, v_h)_h := \sum_{E \in \mathcal{T}_h} \bar{g}|_E \sum_{i=1}^{m_E} v^{\nu_i} \omega_E^i, \quad (16)$$

where ν_1, \dots, ν_{m_E} are the vertices of E , $\bar{g}|_E := \frac{1}{|E|} \int_E g$, and $\omega_E^1, \dots, \omega_E^{m_E}$ are positive weights such that

$$\int_E p_1 = \sum_{i=1}^{m_E} p_1(\nu_i) \omega_E^i$$

for all linear functions p_1 . The loading term above is an approximation of

$$(g, v_h)_h \sim \int_{\Omega} g \tilde{v}.$$

Then, the discretization of Problem 1 reads:

Method 1 *Given $g \in L^2(\Omega)$, find $(\beta_h, w_h) \in H_h \times W_h$ such that*

$$a_h(\beta_h, \eta_h) + \kappa t^{-2} [\nabla_h w_h - \Pi_h \beta_h, \nabla_h v_h - \Pi_h \eta_h]_{\Gamma_h} = (g, v_h)_h$$

for all $(\eta_h, v_h) \in H_h \times W_h$.

In order to extend the method to the free vibration problem, we introduce the following mass bilinear form in $H_h \times W_h$

$$m_h(\beta_h, w_h; \eta_h, v_h) = \sum_{E \in \mathcal{T}_h} m_h^E(\beta_h, w_h; \eta_h, v_h) \quad (17)$$

for all $\beta_h, \eta_h \in H_h$ and $w_h, v_h \in W_h$, where the local forms

$$m_h^E(\beta_h, w_h; \eta_h, v_h) = \sum_{i=1}^{m_E} w^{\nu_i} v^{\nu_i} \omega_E^i + \frac{t^2}{12} \sum_{i=1}^{m_E} (\beta^{\nu_i} \cdot \eta^{\nu_i}) \omega_E^i.$$

Then, the discretization of Problem 2 reads:

Method 2 *Find $\lambda_h \in \mathbb{R}$ and $(\beta_h, w_h) \in H_h \times W_h$ such that*

$$a_h(\beta_h, \eta_h) + \kappa t^{-2} [\nabla_h w_h - \Pi_h \beta_h, \nabla_h v_h - \Pi_h \eta_h]_{\Gamma_h} = \lambda_h m_h(\beta_h, w_h; \eta_h, v_h)$$

for all $(\eta_h, v_h) \in H_h \times W_h$.

Finally, in order to discretize the buckling problem we introduce a discrete bilinear form

$$b_h(w_h, v_h) = \sum_{E \in \mathcal{T}_h} b_h^E(w_h, v_h) \quad \forall w_h, v_h \in W_h, \quad (18)$$

where $b_h^E(\cdot, \cdot)$ is a symmetric bilinear form on each element E , mimicking

$$b_h^E(w_h, v_h) \sim \int_E (\boldsymbol{\sigma} \nabla \tilde{w}_h) \cdot \nabla \tilde{v}_h.$$

We assume for simplicity that the stress datum $\boldsymbol{\sigma}$ is piecewise constant on the mesh, a condition that can also be considered as an approximation of a given data. We require that the local bilinear forms $b_h^E(\cdot, \cdot)$ satisfy the following stability and consistency conditions.

(S1_b) There exists a positive constant \hat{c} independent of h such that, for every $v_h \in W_h$ and each $E \in \mathcal{T}_h$, we have

$$b_h^E(v_h, v_h) \leq \hat{c} \|v_h\|_{W_h, E}^2. \quad (19)$$

(S2_b) For every element E , every scalar linear function p_1 on E , and every $v_h \in W_h$, it holds

$$b_h^E((p_1)_I, v_h) = \sum_{e \in \mathcal{E}_h^E} (\boldsymbol{\sigma} \nabla p_1 \cdot \mathbf{n}_E^e) \frac{|e|}{2} [v^{v_1} + v^{v_2}], \quad (20)$$

where we recall that $\boldsymbol{\sigma}|_E \in \mathbb{R}^{2 \times 2}$ is constant and symmetric.

Such a condition asserts that the discrete bilinear form is exact when tested on linear functions. We also remark that for the form $b_h^E(\cdot, \cdot)$ we *do not* require any lower bound, such as the one in (14). Indeed, assuming a lower bound condition for $b_h^E(\cdot, \cdot)$ would be unnatural, since the stress datum $\boldsymbol{\sigma}$ can be a *singular* second-order tensor.

The discretization of Problem 3 then reads:

Method 3 Find $\lambda_h^{bp} \in \mathbb{R}$ and $(\boldsymbol{\beta}_h, w_h) \in H_h \times W_h$ such that

$$a_h(\boldsymbol{\beta}_h, \boldsymbol{\eta}_h) + \kappa t^{-2} [\nabla_h w_h - \Pi_h \boldsymbol{\beta}_h, \nabla_h v_h - \Pi_h \boldsymbol{\eta}_h]_{\Gamma_h} = \lambda_h^{bp} b_h(w_h, v_h)$$

for all $(\boldsymbol{\eta}_h, v_h) \in H_h \times W_h$.

3.6 Implementation of the method

In this section we describe explicitly how to build the local bilinear forms appearing in the previous sections.

In what follows $m = m(E) \in \mathbb{N}$ will indicate the number of vertices of the polygon E . We number the vertices in counterclockwise sense as $\mathbf{v}_1, \dots, \mathbf{v}_m$ and analogously for the edges $\mathbf{e}_1, \dots, \mathbf{e}_m$, so that \mathbf{v}_j and \mathbf{v}_{j+1} are the endpoints of edge \mathbf{e}_j , $j = 1, 2, \dots, m$. Note that here and in the sequel all such indexes are considered modulus m , so that the index $m+1$ is identified with the index 1. There are a total of $3m$ local degrees of freedom associated to each element of the mesh, three for each vertex. We order such local degrees of freedom first with all rotations and then all deflections, ordered as the vertices

$$\{ \boldsymbol{\eta}_E^{v_1}, \boldsymbol{\eta}_E^{v_2}, \dots, \boldsymbol{\eta}_E^{v_m}, v_E^{v_1}, v_E^{v_2}, \dots, v_E^{v_m} \},$$

where $(\boldsymbol{\eta}_E, v_E) \in H_h|_E \times W_h|_E$.

The final local bilinear forms $\mathbb{M} = \mathbb{M}(E) \in \mathbb{R}^{3m \times 3m}$ associated to each element E will be the sum of two parts

$$\mathbb{M} = \mathbb{M}_1 + \kappa t^{-2} \mathbb{M}_2, \quad (21)$$

the first one being associated to the $a_h(\cdot, \cdot)$ term and the second one to the shear energy term. Once the elemental matrices \mathbb{M} are built, the global stiffness matrix is implemented with a standard assembly procedure as in classical finite elements.

3.6.1 Matrix for the bilinear form $a_h(\cdot, \cdot)$

We start from the bilinear form $a_h(\cdot, \cdot)$, which is the sum of local bilinear forms that we express as matrices $\mathbf{M} = \mathbf{M}(E) \in \mathbb{R}^{2m \times 2m}$

$$a_h^E(\boldsymbol{\beta}_E, \boldsymbol{\eta}_E) = \boldsymbol{\beta}_E^T \mathbf{M} \boldsymbol{\eta}_E \quad \forall E \in \mathcal{T}_h, \quad \forall \boldsymbol{\beta}_E, \boldsymbol{\eta}_E \in H_h|_E.$$

The first and main step is to build the matrix \mathbf{M} . With this purpose we introduce the matrices $\mathbf{N} = \mathbf{N}(E)$ and $\mathbf{R} = \mathbf{R}(E)$ in $\mathbb{R}^{2m \times 6}$. Note again that for ease of notation we do not make explicit the dependence on the involved matrices from E . Let $\mathbf{q}_1, \dots, \mathbf{q}_6$ be the following basis for the first order vector polynomials (with 2 components) defined on E :

$$\mathbf{q}_1 = \begin{pmatrix} 1 \\ 0 \end{pmatrix}, \quad \mathbf{q}_2 = \begin{pmatrix} 0 \\ 1 \end{pmatrix}, \quad \mathbf{q}_3 = \begin{pmatrix} \bar{y} \\ -\bar{x} \end{pmatrix}, \quad \mathbf{q}_4 = \begin{pmatrix} \bar{x} \\ \bar{y} \end{pmatrix}, \quad \mathbf{q}_5 = \begin{pmatrix} \bar{x} \\ \bar{y} \end{pmatrix}, \quad \mathbf{q}_6 = \begin{pmatrix} \bar{x} \\ -\bar{y} \end{pmatrix}.$$

Then, the six columns $\mathbf{N}_1, \dots, \mathbf{N}_6$ of \mathbf{N} are vectors in \mathbb{R}^{2m} defined by the interpolation of the polynomials $\mathbf{q}_1, \dots, \mathbf{q}_6$ into the space $H_h|_E$ (see (4))

$$\mathbf{N}_j = (\mathbf{q}_j)_{\mathbf{I}, E}$$

so that for $1 \leq i \leq m$ and $1 \leq j \leq 6$

$$\begin{pmatrix} \mathbf{N}_{2i-1, j} \\ \mathbf{N}_{2i, j} \end{pmatrix} = \mathbf{q}_j(\mathbf{v}_i).$$

The columns of the matrix \mathbf{N} thus represent the linear polynomials \mathbf{q}_j written in terms of the degrees of freedom of $H_h|_E$.

The columns \mathbf{R}_j of the matrix \mathbf{R} are instead defined as the vectors in \mathbb{R}^{2m} associated to the right hand side of the consistency condition (S2_a), computed with respect to the polynomials \mathbf{q}_j , $j = 1, \dots, 6$. In other words \mathbf{R}_j is the unique vector in \mathbb{R}^{2m} such that for all $\boldsymbol{\eta}_E \in H_h|_E \equiv \mathbb{R}^{2m}$

$$(\mathbf{R}_j)^T \boldsymbol{\eta}_E = \sum_{i=1}^m (\mathcal{C}\varepsilon(\mathbf{q}_j) \mathbf{n}_E^{e_i}) \cdot \left(\frac{|e_i|}{2} [\boldsymbol{\eta}_E^{v_i} + \boldsymbol{\eta}_E^{v_{i+1}}] \right)$$

see equation (S2_a). Note that, since $\varepsilon(\mathbf{q}_j) = \mathbf{0}$ for $j = 1, 2, 3$, the first three columns $\mathbf{R}_1, \mathbf{R}_2, \mathbf{R}_3$ of \mathbf{R} have all zero entries.

From the definition of the vectors \mathbf{N}_j and \mathbf{R}_j , it is clear that the consistency condition (S2_a) translates into the algebraic condition

$$\mathbf{M} \mathbf{N}_j = \mathbf{R}_j \quad j = 1, \dots, 6 \quad \Leftrightarrow \quad \mathbf{M} \mathbf{N} = \mathbf{R}. \quad (22)$$

We therefore introduce the matrix $\mathbf{K} \in \mathbb{R}^{6 \times 6}$ defined by

$$\mathbf{K} = \mathbf{N}^T \mathbf{R} = \mathbf{R}^T \mathbf{N}.$$

It is easy to check that such matrix is symmetric and semi-positive definite. Moreover, it is of the form

$$\mathbf{K} = \begin{pmatrix} \mathbf{0}_{3 \times 3} & \mathbf{0}_{3 \times 3} \\ \mathbf{0}_{3 \times 3} & \mathbf{K}_\star \end{pmatrix}$$

with \mathbf{K}_\star positive definite. Therefore is it immediate to compute the pseudo inverse of \mathbf{K}

$$\mathbf{K}^\dagger = \begin{pmatrix} \mathbf{0}_{3 \times 3} & \mathbf{0}_{3 \times 3} \\ \mathbf{0}_{3 \times 3} & \mathbf{K}_\star^{-1} \end{pmatrix}.$$

We are now ready to define the local matrix \mathbf{M} . Let \mathbf{P} be a projection on the space orthogonal to the columns of \mathbf{N}

$$\mathbf{P} = \mathbb{I}_{2m \times 2m} - \mathbf{N}(\mathbf{N}^T \mathbf{N})^{-1} \mathbf{N}^T$$

with $\mathbb{I}_{2m \times 2m}$ the identity matrix. We then set

$$\mathbf{M} = \mathbf{R} \mathbf{K}^\dagger \mathbf{R}^T + \alpha \mathbf{P}$$

with $\alpha \in \mathbb{R}$ any positive number, typically scaled as the trace of the first part of the matrix. Then, it is immediate to check that \mathbf{M} satisfies the consistency condition (22). Moreover, the positivity up to the kernel is easy to check, while the uniform positivity represented by the stability condition (S1_a) can be proved with the techniques shown in [20, 6].

Finally, note that the matrix $\mathbf{M} \in \mathbb{R}^{2m \times 2m}$ is defined only with respect to the rotation degrees of freedom, since the bilinear form $a_h(\cdot, \cdot)$ is independent of the deflection variable. When it comes to build the local matrix $\mathbb{M}_1 \in \mathbb{R}^{3m \times 3m}$ appearing in (21) one simply needs to introduce the restriction matrix $\mathbf{S} \in \mathbb{R}^{3m \times 2m}$

$$\mathbf{S} = \begin{pmatrix} \mathbb{I}_{2m \times 2m} \\ \mathbf{0}_{m \times 2m} \end{pmatrix}$$

and set

$$\mathbb{M}_1 = \mathbf{S} \mathbf{M} \mathbf{S}^T.$$

3.6.2 Matrix for the shear term

The local matrices for the shear part are obtained as a product of matrices representing the operators and bilinear forms that appear in the second term of the left hand side of Method 1. We therefore start building a matrix $\overline{\mathbf{M}} = \overline{\mathbf{M}}(E) \in \mathbb{R}^{m \times m}$ that represents the local scalar product

$$[\boldsymbol{\gamma}_E, \boldsymbol{\delta}_E]_{\Gamma_h, E} = \boldsymbol{\gamma}_E^T \overline{\mathbf{M}} \boldsymbol{\delta}_E \quad \forall \boldsymbol{\gamma}_E, \boldsymbol{\delta}_E \in \Gamma_h|_E.$$

We order the m degrees of freedom of $\Gamma_h|_E$ as the edges of E . The construction follows the same philosophy as in the previous section and therefore is presented more briefly. Now, the two columns of the matrix $\overline{\mathbf{N}} \in \mathbb{R}^{m \times 2}$ are defined by

$$\overline{\mathbf{N}}_j = (\mathbf{curl} \, q_j)_{\Pi, E} \quad j = 1, 2,$$

where the sub-index Π represents the interpolation operator shown in (5) and q_1, q_2 denote the following basis of the (zero average) linear polynomials on E

$$q_1 = \bar{x}, \quad q_2 = \bar{y}.$$

Analogously, the matrix $\overline{\mathbf{R}} \in \mathbb{R}^{m \times 2}$ is defined through its columns as the right hand side of (S2)

$$(\overline{\mathbf{R}}_j)^T \boldsymbol{\delta}_E = - \sum_{i=1}^m \delta_E^{\mathbf{e}_i} \int_{\mathbf{e}_i} q_j \quad \forall j = 1, 2, \quad \forall \boldsymbol{\delta}_E \in \Gamma_h|_E \equiv \mathbb{R}^m,$$

where we neglected the rot_{Γ_h} part since q_1 and q_2 have zero average on E . Again, we need to introduce $\bar{\mathbf{K}} \in \mathbb{R}^{2 \times 2}$ given by

$$\bar{\mathbf{K}} = \bar{\mathbf{N}}^T \bar{\mathbf{R}} = \bar{\mathbf{R}}^T \bar{\mathbf{N}}$$

that is easily shown to be positive definite and symmetric. We can therefore finally set

$$\bar{\mathbf{M}} = \bar{\mathbf{R}} (\bar{\mathbf{K}})^{-1} \bar{\mathbf{R}}^T + \alpha \bar{\mathbf{P}}$$

with $\alpha \in \mathbb{R}^+$ and the projection matrix

$$\bar{\mathbf{P}} = \mathbb{I}_{m \times m} - \bar{\mathbf{N}} (\bar{\mathbf{N}}^T \bar{\mathbf{N}})^{-1} \bar{\mathbf{N}}^T.$$

The consistency condition $\bar{\mathbf{M}} \bar{\mathbf{N}} = \bar{\mathbf{R}}$ follows by construction while the stability can be derived with the results in [20].

The local matrix \mathbb{M}_2 appearing in (21) can be built combining $\bar{\mathbf{M}}$ with a matrix $\mathbf{C} = \mathbf{C}(E) \in \mathbb{R}^{m \times 3m}$ representing the ∇_h and Π_h operators that appear in Method 1. We therefore set

$$\mathbf{C} = (-\mathbf{C}_1 \ \mathbf{C}_2)$$

with the matrix $\mathbf{C}_1 = \mathbf{C}_1(E) \in \mathbb{R}^{m \times 2m}$ representing the Π_h operator

$$\mathbf{C}_1 = \frac{1}{2} \begin{pmatrix} (\mathbf{t}_E^{\mathbf{e}_1})^T & (\mathbf{t}_E^{\mathbf{e}_1})^T & \mathbf{0}_{1 \times 2} & \mathbf{0}_{1 \times 2} & \dots & \mathbf{0}_{1 \times 2} \\ \mathbf{0}_{1 \times 2} & (\mathbf{t}_E^{\mathbf{e}_2})^T & (\mathbf{t}_E^{\mathbf{e}_2})^T & \mathbf{0}_{1 \times 2} & \dots & \mathbf{0}_{1 \times 2} \\ \mathbf{0}_{1 \times 2} & \mathbf{0}_{1 \times 2} & (\mathbf{t}_E^{\mathbf{e}_3})^T & (\mathbf{t}_E^{\mathbf{e}_3})^T & \dots & \mathbf{0}_{1 \times 2} \\ \vdots & \vdots & \vdots & \vdots & \vdots & \vdots \\ (\mathbf{t}_E^{\mathbf{e}_m})^T & \mathbf{0}_{1 \times 2} & \dots & \mathbf{0}_{1 \times 2} & \mathbf{0}_{1 \times 2} & (\mathbf{t}_E^{\mathbf{e}_m})^T \end{pmatrix},$$

and the matrix $\mathbf{C}_2 = \mathbf{C}_2(E) \in \mathbb{R}^{m \times m}$ representing the ∇_h operator

$$\mathbf{C}_2 = \begin{pmatrix} -|\mathbf{e}_1|^{-1} & |\mathbf{e}_1|^{-1} & 0 & 0 & \dots & 0 \\ 0 & -|\mathbf{e}_2|^{-1} & |\mathbf{e}_2|^{-1} & 0 & \dots & 0 \\ 0 & 0 & -|\mathbf{e}_3|^{-1} & |\mathbf{e}_3|^{-1} & \dots & 0 \\ \vdots & \vdots & \vdots & \vdots & \vdots & \vdots \\ -|\mathbf{e}_m|^{-1} & 0 & \dots & 0 & 0 & |\mathbf{e}_m|^{-1} \end{pmatrix}.$$

Finally, the local matrices for the shear part are given by

$$\mathbb{M}_2 = \mathbf{C}^T \bar{\mathbf{M}} \mathbf{C}.$$

3.6.3 Right hand sides

The *loading term* for the source problem in Method 1 follows immediately from (16). One gets the local right hand vectors $\mathbf{b} = \mathbf{b}(E) \in \mathbb{R}^{3m}$ defined by

$$\mathbf{b}_j = \begin{cases} 0 & \text{if } j = 1, 2, \dots, 2m \\ \bar{g}|_E \omega_E^{(j-2m)} & \text{if } j = 2m + 1, 2m + 2, \dots, 3m, \end{cases}$$

that are then assembled as usual into the global load vector.

The *mass matrix* for the free vibration problem in Method 2, associated to the bilinear form (17) is built again by a standard assembly procedure. The local mass matrices $\mathbf{D} = \mathbf{D}(E) \in \mathbb{R}^{3m \times 3m}$ associated to the elemental mass bilinear forms

$$m_h^E(\boldsymbol{\beta}_E, w_E; \boldsymbol{\eta}_E, v_E) = (\boldsymbol{\beta}_E, w_E)^T \mathbf{D}(\boldsymbol{\eta}_E, v_E) \quad \forall E \in \mathcal{T}_h, \\ \forall \boldsymbol{\beta}_E, \boldsymbol{\eta}_E \in H_h|_E, \forall w_E, v_E \in W_h|_E$$

are diagonal and defined by

$$D_{ii} = \begin{cases} t^2 \omega_E^{\lceil i/2 \rceil} / 12 & \text{if } i = 1, 2, \dots, 2m \\ \omega_E^{(i-2m)} & \text{if } i = 2m + 1, 2m + 2, \dots, 3m \end{cases}$$

where the symbol $\lceil \cdot \rceil$ stands for a round up to the nearest integer.

The *stress matrix* for the buckling problem in Method 3, associated to the bilinear form (18) is also built as the sum of local matrices $\widehat{\mathbf{B}} = \widehat{\mathbf{B}}(E) \in \mathbb{R}^{m \times m}$

$$b_h^E(w_E, v_E) = w_E^T \widehat{\mathbf{B}} v_E \quad \forall w_E, v_E \in W_h|_E.$$

Note that the symmetric tensor $\boldsymbol{\sigma} \in \mathbb{R}^{2 \times 2}$ that appears in (S2_b) can have either rank 2 or rank 1. In order to build the matrix $\widehat{\mathbf{B}}$, we start introducing $\{\hat{q}_1, \hat{q}_2, \hat{q}_3\}$ a basis for the linear polynomials on E , such that $\hat{q}_1 = 1$ and \hat{q}_2, \hat{q}_3 have zero integral on E . Moreover, if $\text{rank}(\boldsymbol{\sigma}) = 1$, we also require that $\nabla \hat{q}_2 \in \text{Ker}(\boldsymbol{\sigma})$. We then define as usual the auxiliary matrices $\widehat{\mathbf{N}} = \widehat{\mathbf{N}}(E) \in \mathbb{R}^{m \times 3}$ and $\widehat{\mathbf{R}} = \widehat{\mathbf{R}}(E) \in \mathbb{R}^{m \times 3}$ through its columns. We set

$$\widehat{\mathbf{N}}_j = (\hat{q}_j)_{\mathbf{I}, E}, \quad j = 1, 2, 3,$$

where the sub-index \mathbf{I} denotes the interpolation operator in (3), and define $\widehat{\mathbf{R}}_j$ as the unique vector in \mathbb{R}^m such that

$$\widehat{\mathbf{R}}_j^T v_E = \sum_{i=1}^m (\boldsymbol{\sigma} \nabla \hat{q}_j \cdot \mathbf{n}_E^{\mathbf{e}_i}) \frac{|\mathbf{e}_j|}{2} [v_E^{v_i} + v_E^{v_i+1}] \quad \forall j = 1, 2, 3, \forall v_E \in W_h|_E \equiv \mathbb{R}^m$$

in accordance with (S2_b). Note that clearly $\widehat{\mathbf{R}}_1$ is null, and that, if $\text{rank}(\boldsymbol{\sigma}) = 1$ also $\widehat{\mathbf{R}}_2$ is null. One then defines as usual the semi-positive definite and symmetric matrix $\widehat{\mathbf{K}} = \widehat{\mathbf{K}}(E) \in \mathbb{R}^{3 \times 3}$

$$\widehat{\mathbf{K}} = \widehat{\mathbf{R}}^T \widehat{\mathbf{N}} = \widehat{\mathbf{N}}^T \widehat{\mathbf{R}}.$$

Since $\widehat{\mathbf{K}}$ is block diagonal, with the first block of zeros and the second invertible, it is immediate to compute the pseudo inverse matrix $\widehat{\mathbf{K}}^\dagger$, in a way similar to the one used for \mathbf{K} in Section 3.6.1. Then, we introduce $\widehat{\mathbf{B}} = \widehat{\mathbf{B}}(E) \in \mathbb{R}^{m \times m}$

$$\widehat{\mathbf{B}} = \widehat{\mathbf{R}} (\widehat{\mathbf{K}})^\dagger \widehat{\mathbf{R}}^T + \alpha \widehat{\mathbf{P}}$$

with $\alpha \in \mathbb{R}$ non negative and the projection matrix $\widehat{\mathbf{P}} = \mathbb{I}_{m \times m} - \widehat{\mathbf{N}} (\widehat{\mathbf{N}}^T \widehat{\mathbf{N}})^{-1} \widehat{\mathbf{N}}^T$. Note that, since no global coercivity conditions are required, differently from the previous matrices also the choice $\alpha = 0$ can be taken.

Finally, note that the matrix $\widehat{\mathbf{B}} \in \mathbb{R}^{m \times m}$ is defined only with respect to the deflection degrees of freedom, since the bilinear form $b_h(\cdot, \cdot)$ is independent of the rotation variable. The remaining entries in the assembled (right hand side) stress matrix associated to Method 3 can be simply filled with zeros.

4 Numerical results

The numerical method analyzed has been implemented in a MATLAB code.

For all the computations we took $\Omega := (0, 1)^2$, for the Young modulus we choose: $E = 1$.

We have tested the method by using different meshes. We report the results obtained using the families of meshes shown in Figure 1 to Figure 7.

- \mathcal{T}_h^1 : Triangular mesh.
- \mathcal{T}_h^2 : Structured hexagonal meshes.
- \mathcal{T}_h^3 : Non-structured hexagonal meshes made of convex hexagons.
- \mathcal{T}_h^4 : Regular subdivisions of the domain in $N \times N$ subsquares.
- \mathcal{T}_h^5 : Trapezoidal meshes which consist of partitions of the domain into $N \times N$ congruent trapezoids, all similar to the trapezoid with vertices $(0, 0)$, $(\frac{1}{2}, 0)$, $(\frac{1}{2}, \frac{2}{3})$, and $(0, \frac{1}{3})$.
- \mathcal{T}_h^6 : Regular polygonal meshes built from \mathcal{T}_h^1 considering the middle point of each edge as a new node on the mesh; note that each element has 6 edges.
- \mathcal{T}_h^7 : Irregular polygonal meshes built from \mathcal{T}_h^6 moving randomly the middle point of each edge; note that these meshes contain non-convex elements.

We have used successive refinements of an initial mesh (see Figure 1 to Figure 7). The refinement parameter N used to label each mesh is the number of elements on each edge of the plate.

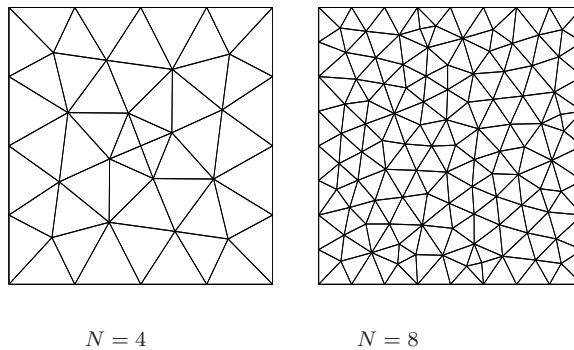


Fig. 1 Square plate: meshes \mathcal{T}_h^1 .

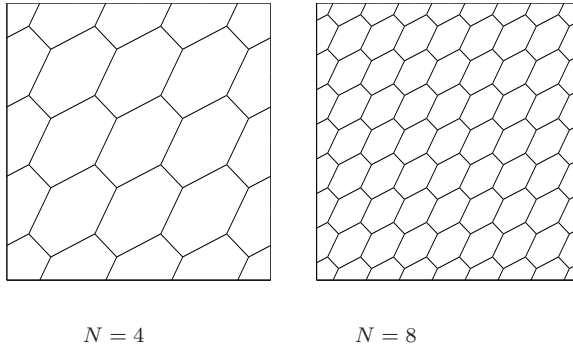


Fig. 2 Square plate: meshes \mathcal{T}_h^2 .

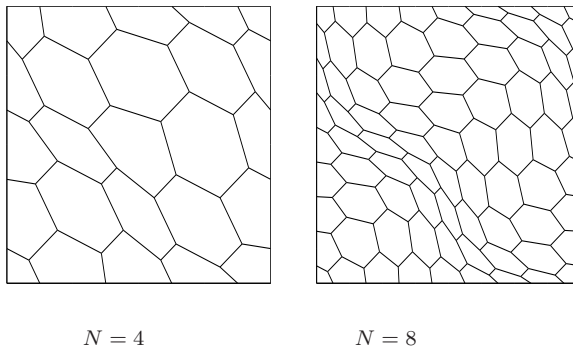


Fig. 3 Square plate: meshes \mathcal{T}_h^3 .

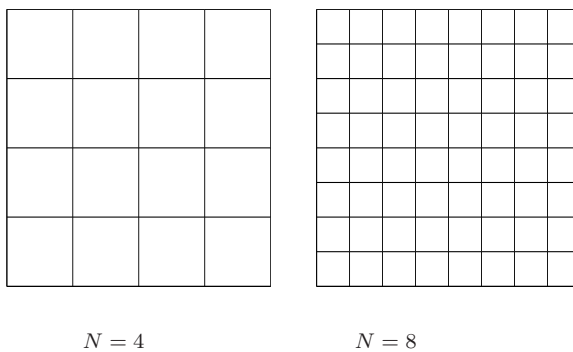


Fig. 4 Square plate: meshes \mathcal{T}_h^4 .

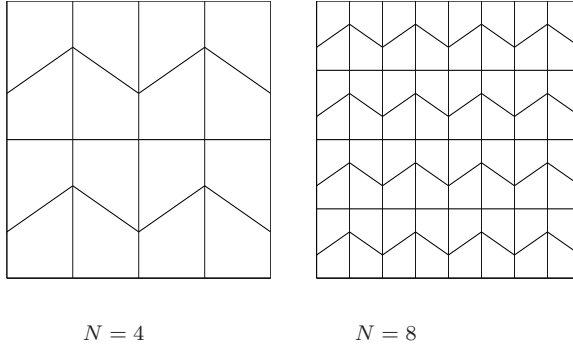


Fig. 5 Square plate: meshes \mathcal{T}_h^5 .

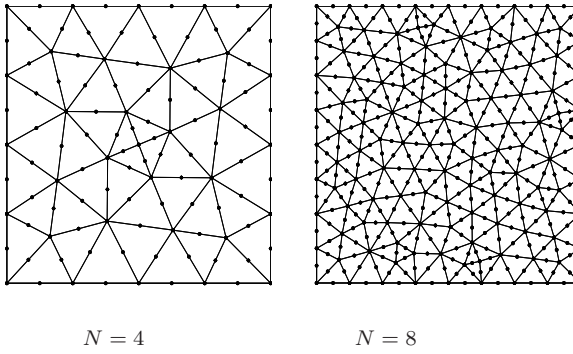


Fig. 6 Square plate: meshes \mathcal{T}_h^6 .

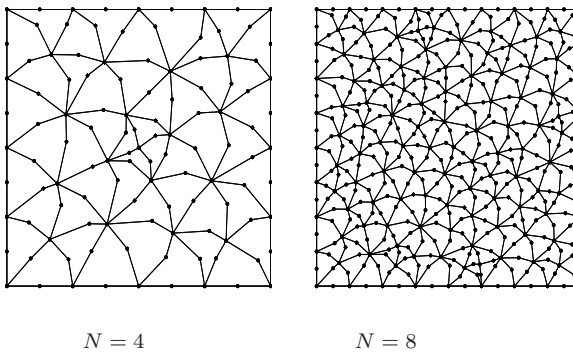


Fig. 7 Square plate: meshes \mathcal{T}_h^7 .

4.1 Source problem

As a test problem we have taken an isotropic and homogeneous plate, clamped on the whole boundary, for which the analytical solution is explicitly known (see [24]).

Choosing the transversal load g as:

$$g(x, y) = \frac{E}{12(1-\nu^2)} \left[12y(y-1)(5x^2-5x+1)(2y^2(y-1)^2 + x(x-1)(5y^2-5y+1)) \right. \\ \left. + 12x(x-1)(5y^2-5y+1)(2x^2(x-1)^2 + y(y-1)(5x^2-5x+1)) \right],$$

the exact solution of the problem is given by:

$$w(x, y) = \frac{1}{3}x^3(x-1)^3y^3(y-1)^3 \\ - \frac{2t^2}{5(1-\nu)} \left[y^3(y-1)^3x(x-1)(5x^2-5x+1) + x^3(x-1)^3y(y-1)(5y^2-5y+1) \right], \\ \beta_1(x, y) = y^3(y-1)^3x^2(x-1)^2(2x-1), \\ \beta_2(x, y) = x^3(x-1)^3y^2(y-1)^2(2y-1).$$

We have used a Poisson ratio $\nu = 0.3$ and a correction factor $k = 5/6$.

The convergence rates for the transverse displacement w and rotations β are shown in the following norms:

$$\mathbf{e}(\beta)_0 := \frac{\max |\beta_{\mathbf{I}} - \beta_h|}{\max |\beta_{\mathbf{I}}|}, \quad \mathbf{e}(w)_0 := \frac{\max |w_{\mathbf{I}} - w_h|}{\max |w_{\mathbf{I}}|}, \quad (23)$$

$$\mathbf{e}(\beta)_1 := \frac{a_h(\beta_{\mathbf{I}} - \beta_h, \beta_{\mathbf{I}} - \beta_h)^{1/2}}{a_h(\beta_{\mathbf{I}}, \beta_{\mathbf{I}})^{1/2}}, \quad \mathbf{e}(w)_1 := \frac{[\nabla_h(w_{\mathbf{I}} - w_h), \nabla_h(w_{\mathbf{I}} - w_h)]_{\Gamma_h}^{1/2}}{[\nabla_h w_{\mathbf{I}}, \nabla_h w_{\mathbf{I}}]_{\Gamma_h}^{1/2}}. \quad (24)$$

In (24) the bilinear forms $a_h(\cdot, \cdot)$ and $[\cdot, \cdot]_{\Gamma_h}$ are exactly the ones defined in (13) and (10), respectively. We notice that it holds:

$$\mathbf{e}(\beta)_1 \sim \frac{\|\beta_{\mathbf{I}} - \beta_h\|_{H_h}}{\|\beta_{\mathbf{I}}\|_{H_h}}, \quad \mathbf{e}(w)_1 \sim \frac{\|w_{\mathbf{I}} - w_h\|_{W_h}}{\|w_{\mathbf{I}}\|_{W_h}}.$$

Therefore, (23) and (24) represent discrete L^∞ and H^1 relative errors, respectively.

Also, we define the experimental rates of convergence (rc) for the errors $\mathbf{e}(\beta)$ and $\mathbf{e}(w)$ by

$$rc(\cdot) := \frac{\log(\mathbf{e}(\cdot)/\mathbf{e}'(\cdot))}{\log(h/h')},$$

where h and h' denote two consecutive meshsizes and \mathbf{e} and \mathbf{e}' , respectively, denote the corresponding errors.

Table 1 shows the convergence history of the Method 1 applied to our test problem with four different family of meshes. Table 2 shows instead an analysis for various thicknesses in order to assess the locking free nature of the proposed method.

Table 1 Convergence analysis for $t = 0.01$. Errors and experimental rates of convergence for variables β and w .

Mesh	$1/h$	$e(\beta)_0$	$rc(\beta)_0$	$e(w)_0$	$rc(w)_0$	$e(\beta)_1$	$rc(\beta)_1$	$e(w)_1$	$rc(w)_1$
\mathcal{T}_h^2	8	5.018e-2	–	2.641e-2	–	9.700e-2	–	6.480e-2	–
	16	1.103e-2	2.19	9.522e-3	1.47	2.967e-2	1.71	1.988e-2	1.70
	32	2.788e-3	1.98	2.761e-3	1.79	8.992e-3	1.72	5.404e-3	1.88
	64	7.166e-4	1.96	7.351e-4	1.91	2.886e-3	1.64	1.403e-3	1.95
	128	1.814e-4	1.98	1.891e-4	1.96	1.010e-3	1.51	3.572e-4	1.97
\mathcal{T}_h^3	8	7.137e-2	–	5.208e-2	–	1.325e-1	–	8.680e-2	–
	16	3.505e-2	1.03	2.095e-2	1.31	5.465e-2	1.28	3.303e-2	1.39
	32	1.131e-2	1.63	6.219e-3	1.75	1.793e-2	1.61	9.714e-3	1.77
	64	3.108e-3	1.86	1.634e-3	1.93	5.619e-3	1.67	2.571e-3	1.92
	128	7.991e-4	1.96	4.156e-4	1.98	1.846e-3	1.61	6.571e-4	1.97
\mathcal{T}_h^4	8	3.224e-2	–	6.519e-2	–	4.370e-2	–	9.599e-2	–
	16	8.156e-3	1.98	1.605e-2	2.02	1.132e-2	1.95	2.518e-2	1.93
	32	2.051e-3	1.99	3.997e-3	2.00	2.866e-3	1.98	6.365e-3	1.98
	64	5.138e-4	1.99	9.983e-4	2.00	7.188e-4	2.00	1.595e-3	2.00
	128	1.285e-4	1.99	2.496e-4	2.00	1.798e-4	2.00	3.991e-4	2.00
\mathcal{T}_h^5	8	7.190e-2	–	1.057e-1	–	1.949e-1	–	1.318e-1	–
	16	1.677e-2	2.10	2.331e-2	2.18	1.127e-1	0.79	4.339e-2	1.60
	32	3.509e-3	2.26	5.201e-3	2.16	4.213e-2	1.42	1.080e-2	2.01
	64	5.942e-4	2.56	1.221e-3	2.09	1.127e-2	1.90	2.380e-3	2.18
	128	1.504e-4	1.98	2.896e-4	2.08	3.802e-3	1.57	5.516e-4	2.11

We observe from Table 1 that a clear rate of convergence $O(h^2)$ is attained for β and w for all family of meshes in the discrete L^∞ norm. Moreover, a rate of convergence $O(h^{3/2})$ for β and $O(h^2)$ for w for all family of meshes in the discrete H^1 norm have been obtained. Actually, the computation of β using meshes \mathcal{T}_h^4 seems to be superconvergent.

Table 2 Locking-free analysis for variable w ($e(w)_1$)

Mesh	$1/h$	$t=1.0e-2$	$t=1.0e-3$	$t=1.0e-4$	$t=1.0e-5$
\mathcal{T}_h^1	8	2.040179e-1	9.381597e-1	9.993307e-1	9.999933e-1
	16	2.975046e-2	3.790016e-1	9.773959e-1	9.997674e-1
	32	4.320781e-3	4.271249e-2	5.521358e-1	9.902023e-1
	64	8.636150e-4	5.651503e-3	8.549716e-2	7.775880e-1
\mathcal{T}_h^3	8	8.680034e-2	8.648290e-2	8.647974e-2	8.647905e-2
	16	3.303805e-2	3.289787e-2	3.289649e-2	3.289827e-2
	32	9.714549e-3	9.670538e-3	9.670075e-3	9.671654e-3
	64	2.571361e-3	2.558931e-3	2.558797e-3	2.555879e-3
\mathcal{T}_h^4	8	9.598706e-2	9.605054e-2	9.605176e-2	9.605118e-2
	16	2.518265e-2	2.518620e-2	2.518623e-2	2.518663e-2
	32	6.364552e-3	6.364126e-3	6.364108e-3	6.364647e-3
	64	1.595350e-3	1.595135e-3	1.595115e-3	1.595949e-3
\mathcal{T}_h^6	8	7.471495e-2	7.399270e-2	7.398561e-2	7.398560e-2
	16	2.223311e-2	2.217105e-2	2.217068e-2	2.217124e-2
	32	6.155689e-3	6.173926e-3	6.174458e-3	6.176650e-3
	64	1.268306e-3	1.308765e-3	1.309856e-3	1.311575e-3
\mathcal{T}_h^7	8	8.776844e-2	8.835775e-2	8.547591e-2	8.870029e-2
	16	3.128646e-2	3.002581e-2	3.088068e-2	2.990004e-2
	32	8.776518e-3	8.804238e-3	9.034351e-3	8.770496e-3
	64	1.925048e-3	2.025191e-3	2.042556e-3	1.966998e-3

We observe from Table 2 that our Method 1 lead to wrong result *only* for triangular meshes \mathcal{T}_h^1 , when the thickness of the plate is small. For any other family of meshes the method is locking-free. We also note that adding the middle point of each edge as a new node on any triangular mesh, the method is locking free, see row corresponding to \mathcal{T}_h^1 and \mathcal{T}_h^6 .

Remark 3 We note that the different behavior among the triangular mesh \mathcal{T}_h^1 and the remaining grids is not surprising. Indeed, \mathcal{T}_h^1 resembles a plain $P1$ element, that is known to suffer from locking in the plate finite element literature, unless edge bubbles are added to the rotations (see also Remark 1). Moreover, the analysis of [11] does not apply to the \mathcal{T}_h^1 meshes since the $P1/P0$ element is not stable for the Stokes problem. Instead, meshes \mathcal{T}_h^2 , \mathcal{T}_h^3 fall into the hypotheses of the convergence theorem of [7], see Remark 4 of [11]. Meshes \mathcal{T}_h^4 , \mathcal{T}_h^5 have a strong connection with the MITC4 finite element for plates that is known to be stable. Finally, meshes \mathcal{T}_h^6 , \mathcal{T}_h^7 again fall into the convergent cases considered in [7] and thus stable also for Reissner-Mindlin (see [11]).

4.2 Free vibration of plates

The effectiveness of the MDF method for free vibration analysis are demonstrated by examples with different thickness and different boundary conditions.

We have computed approximations of the free vibration angular frequencies $\omega^h = t\sqrt{\frac{\lambda_k}{\rho}}$. In order to compare our results with those in [25,27,28,30], a non-dimensional frequency parameter is defined as:

$$\omega_{mn} := \omega_{mn}^h L \sqrt{\frac{2(1+\nu)\rho}{E}},$$

here ω_{mn}^h are the computed frequencies, where m and n are the numbers of half-waves in the modal shapes in the x and y directions, respectively. L is the plate side length.

We have considered a square plate of side length $L = 1$ and $\rho = 1$ and three different thickness $t = 0.1$, $t = 0.01$ and $t=1.0e-5$. We have also considered three different types of boundary conditions: a clamped plate (denote by CCCC), a simply supported plate (denote by SSSS), and a plate with a free edge (with three clamped edges and the fourth free, we denote by CCCF).

In the following numerical tests, we show the results for the four lowest vibration frequencies. We tested also higher frequencies with similar results.

Tables 3 and 4 show the four lowest vibration frequencies computed by Method 2 with successively refined meshes of each type for a clamped plate with thickness $t = 0.1$ and $t = 0.01$, respectively. The table includes orders of convergence, as well as accurate values extrapolated by means of a least-squares fitting. Furthermore, the last two columns show the results reported in [25,27,30]. In every case, we have used a Poisson ratio $\nu = 0.3$ and a correction factor $k = 0.8601$. The reported non-dimensional frequencies are independent of the remaining geometrical and physical parameters, except for the thickness-to-span ratio.

Table 3 Lowest non-dimensional vibration frequencies for a CCCC square plate and $t = 0.1$

Mesh	Mode	$N = 32$	$N = 64$	$N = 128$	Order	Extrap.	[30]	[27]
\mathcal{T}_h^2	ω_{11}	1.5938	1.5918	1.5912	1.84	1.5910	1.591	1.5910
	ω_{21}	3.0458	3.0408	3.0394	1.85	3.0389	3.039	3.0388
	ω_{12}	3.0500	3.0419	3.0397	1.90	3.0389	3.039	3.0388
	ω_{22}	4.2807	4.2675	4.2638	1.85	4.2624	4.263	4.2624
\mathcal{T}_h^3	ω_{11}	1.5958	1.5923	1.5914	1.84	1.5910	1.591	1.5910
	ω_{21}	3.0524	3.0426	3.0399	1.83	3.0388	3.039	3.0388
	ω_{12}	3.0570	3.0438	3.0402	1.88	3.0388	3.039	3.0388
	ω_{22}	4.2903	4.2701	4.2645	1.84	4.2623	4.263	4.2624
\mathcal{T}_h^4	ω_{11}	1.5961	1.5923	1.5914	1.97	1.5910	1.591	1.5910
	ω_{21}	3.0526	3.0424	3.0398	1.98	3.0389	3.039	3.0388
	ω_{12}	3.0526	3.0424	3.0398	1.98	3.0389	3.039	3.0388
	ω_{22}	4.2914	4.2699	4.2644	1.97	4.2625	4.263	4.2624
\mathcal{T}_h^5	ω_{11}	1.5967	1.5925	1.5914	1.98	1.5910	1.591	1.5910
	ω_{21}	3.0527	3.0424	3.0398	1.98	3.0389	3.039	3.0388
	ω_{12}	3.0573	3.0435	3.0401	2.00	3.0389	3.039	3.0388
	ω_{22}	4.2943	4.2705	4.2645	1.98	4.2625	4.263	4.2624

Table 4 Lowest non-dimensional vibration frequencies for a CCCC square plate and $t = 0.01$

Mesh	Mode	$N = 32$	$N = 64$	$N = 128$	Order	Extrap.	[30]	[25]
\mathcal{T}_h^2	ω_{11}	0.1757	0.1755	0.1754	1.89	0.1754	0.1754	0.1754
	ω_{21}	0.3582	0.3576	0.3574	1.87	0.3574	0.3574	0.3576
	ω_{12}	0.3587	0.3577	0.3575	1.91	0.3574	0.3574	0.3576
	ω_{22}	0.5289	0.5272	0.5267	1.86	0.5265	0.5264	0.5274
\mathcal{T}_h^3	ω_{11}	0.1759	0.1755	0.1754	1.87	0.1754	0.1754	0.1754
	ω_{21}	0.3590	0.3578	0.3575	1.84	0.3574	0.3574	0.3576
	ω_{12}	0.3596	0.3580	0.3575	1.87	0.3574	0.3574	0.3576
	ω_{22}	0.5304	0.5276	0.5268	1.83	0.5265	0.5264	0.5274
\mathcal{T}_h^4	ω_{11}	0.1759	0.1755	0.1754	1.99	0.1754	0.1754	0.1754
	ω_{21}	0.3593	0.3579	0.3575	2.00	0.3574	0.3574	0.3576
	ω_{12}	0.3593	0.3579	0.3575	2.00	0.3574	0.3574	0.3576
	ω_{22}	0.5306	0.5275	0.5268	1.99	0.5265	0.5264	0.5274
\mathcal{T}_h^5	ω_{11}	0.1762	0.1756	0.1754	2.21	0.1754	0.1754	0.1754
	ω_{21}	0.3597	0.3579	0.3575	2.10	0.3574	0.3574	0.3576
	ω_{12}	0.3613	0.3582	0.3576	2.33	0.3574	0.3574	0.3576
	ω_{22}	0.5323	0.5278	0.5268	2.16	0.5265	0.5264	0.5274

It can be seen from Tables 3 and 4 that our method converges with a quadratic order.

Table 5 shows the four lowest vibration frequencies computed by Method 2 with successively refined meshes of each type for a clamped plate with $t=1.0e-5$. The table includes orders of convergence, as well as accurate values extrapolated by means of a least-squares fitting. In every case, we have used a Poisson ratio $\nu = 0.3$ and a correction factor $k = 0.8601$. The reported non-dimensional frequencies are independent of the remaining geometrical and physical parameters, except for the thickness-to-span ratio.

Table 5 Lowest non-dimensional vibration frequencies for a CCCC square plate and $t=1.0e-5$

Mesh	Mode	$N = 8$	$N = 16$	$N = 32$	Order	Extrap.
\mathcal{T}_h^1	ω_{11}	0.7653e-1	0.1289e-1	0.1987e-2	2.54	-0.2995e-3
	ω_{21}	0.1972e-0	0.3228e-1	0.4942e-2	2.59	-0.5396e-3
	ω_{12}	0.2230e-0	0.4060e-1	0.5085e-2	2.36	-0.3519e-2
	ω_{22}	0.3915e-0	0.6093e-1	0.9893e-2	2.70	0.7086e-3
\mathcal{T}_h^4	ω_{11}	0.1848e-3	0.1778e-3	0.1761e-3	2.04	0.1756e-3
	ω_{21}	0.3927e-3	0.3661e-3	0.3601e-3	2.15	0.3583e-3
	ω_{12}	0.3927e-3	0.3661e-3	0.3601e-3	2.15	0.3583e-3
	ω_{22}	0.5983e-3	0.5446e-3	0.5321e-3	2.11	0.5284e-3
\mathcal{T}_h^6	ω_{11}	0.1772e-3	0.1760e-3	0.1757e-3	2.10	0.1756e-3
	ω_{21}	0.3634e-3	0.3592e-3	0.3584e-3	2.33	0.3582e-3
	ω_{12}	0.3650e-3	0.3594e-3	0.3584e-3	2.53	0.3582e-3
	ω_{22}	0.5440e-3	0.5312e-3	0.5286e-3	2.30	0.5279e-3
\mathcal{T}_h^7	ω_{11}	0.1779e-3	0.1761e-3	0.1757e-3	1.94	0.1755e-3
	ω_{21}	0.3654e-3	0.3599e-3	0.3585e-3	1.95	0.3580e-3
	ω_{12}	0.3679e-3	0.3600e-3	0.3585e-3	2.40	0.3582e-3
	ω_{22}	0.5489e-3	0.5325e-3	0.5289e-3	2.18	0.5278e-3

It can be seen from Table 5 that as for the source problem, our Method 2 lead to wrong result for triangular meshes \mathcal{T}_h^1 when the thickness of the plate is small, see Remark 3. For any other family of meshes the method is locking free and converges with a quadratic order.

Table 6 shows the four lowest vibration frequencies computed by Method 2 with successively refined meshes of each type for a simply supported plate with thickness $t = 0.01$. The table includes orders of convergence, as well as accurate values extrapolated by means of a least-squares fitting. Furthermore, the last two columns show the results reported in [30, 25]. In every case, we have used a Poisson ratio $\nu = 0.3$ and a correction factor $k = 0.8333$. The reported non-dimensional frequencies are independent of the remaining geometrical and physical parameters, except for the thickness-to-span ratio.

Table 6 Lowest non-dimensional vibration frequencies for a SSSS square plate and $t = 0.01$

Mesh	Mode	$N = 16$	$N = 32$	$N = 64$	Order	Extrap.	[30]	[25]
\mathcal{T}_h^2	ω_{11}	0.0966	0.0963	0.0963	2.04	0.0963	0.0963	0.0963
	ω_{21}	0.2416	0.2408	0.2406	2.07	0.2406	0.2406	0.2406
	ω_{12}	0.2425	0.2411	0.2407	2.02	0.2406	0.2406	0.2406
	ω_{22}	0.3889	0.3858	0.3850	2.00	0.3847	0.3847	0.3848
\mathcal{T}_h^3	ω_{11}	0.0967	0.0964	0.0963	1.96	0.0963	0.0963	0.0963
	ω_{21}	0.2424	0.2410	0.2407	1.91	0.2406	0.2406	0.2406
	ω_{12}	0.2434	0.2413	0.2408	1.93	0.2406	0.2406	0.2406
	ω_{22}	0.3914	0.3865	0.3852	1.92	0.3847	0.3847	0.3848
\mathcal{T}_h^4	ω_{11}	0.0966	0.0964	0.0963	2.00	0.0963	0.0963	0.0963
	ω_{21}	0.2426	0.2411	0.2407	2.02	0.2406	0.2406	0.2406
	ω_{12}	0.2426	0.2411	0.2407	2.02	0.2406	0.2406	0.2406
	ω_{22}	0.3898	0.3860	0.3850	2.01	0.3847	0.3847	0.3848
\mathcal{T}_h^5	ω_{11}	0.0967	0.0964	0.0963	2.01	0.0963	0.0963	0.0963
	ω_{21}	0.2429	0.2411	0.2407	2.07	0.2406	0.2406	0.2406
	ω_{12}	0.2441	0.2414	0.2408	2.09	0.2406	0.2406	0.2406
	ω_{22}	0.3910	0.3863	0.3851	2.01	0.3847	0.3847	0.3848
\mathcal{T}_h^6	ω_{11}	0.0964	0.0963	0.0963	2.82	0.0963	0.0963	0.0963
	ω_{21}	0.2411	0.2406	0.2406	3.79	0.2406	0.2406	0.2406
	ω_{12}	0.2417	0.2407	0.2406	3.82	0.2406	0.2406	0.2406
	ω_{22}	0.3869	0.3850	0.3848	3.40	0.3848	0.3847	0.3848
\mathcal{T}_h^7	ω_{11}	0.0965	0.0963	0.0963	2.53	0.0963	0.0963	0.0963
	ω_{21}	0.2416	0.2408	0.2406	2.35	0.2406	0.2406	0.2406
	ω_{12}	0.2427	0.2408	0.2407	3.48	0.2406	0.2406	0.2406
	ω_{22}	0.3889	0.3854	0.3848	2.61	0.3847	0.3847	0.3848

Table 7 shows the four lowest vibration frequencies computed by Method 2 with successively refined meshes of each type for a plate with a free edge (with three clamped edges and the fourth free) with thickness $t = 0.01$. The table includes orders of convergence, as well as accurate values extrapolated by means of a least-squares fitting. Furthermore, the last two columns show the results reported in [30, 25]. In every case, we have used a Poisson ratio $\nu = 0.3$ and a correction factor $k = 0.8601$. The reported non-dimensional frequencies are independent of the remaining geometrical and physical parameters, except for the thickness-to-span ratio.

Table 7 Lowest non-dimensional vibration frequencies for a CCCF square plate and $t = 0.01$

Mesh	Mode	$N = 32$	$N = 64$	$N = 128$	Order	Extrap.	[30]	[25]
\mathcal{T}_h^4	ω_{11}	0.1215	0.1179	0.1169	1.98	0.1166	0.1166	0.1171
	ω_{21}	0.2030	0.1970	0.1954	1.97	0.1949	0.1949	0.1951
	ω_{12}	0.3358	0.3144	0.3096	2.14	0.3081	0.3083	0.3093
	ω_{22}	0.3884	0.3773	0.3745	1.97	0.3735	0.3736	0.3740
\mathcal{T}_h^5	ω_{11}	0.1199	0.1173	0.1167	2.18	0.1166	0.1166	0.1171
	ω_{21}	0.1986	0.1958	0.1951	2.00	0.1948	0.1949	0.1951
	ω_{12}	0.3264	0.3117	0.3086	2.25	0.3078	0.3083	0.3093
	ω_{22}	0.3791	0.3749	0.3738	1.92	0.3734	0.3736	0.3740
\mathcal{T}_h^6	ω_{11}	0.1177	0.1169	0.1167	2.00	0.1166	0.1166	0.1171
	ω_{21}	0.1967	0.1953	0.1949	2.13	0.1948	0.1949	0.1951
	ω_{12}	0.3134	0.3090	0.3081	2.22	0.3079	0.3083	0.3093
	ω_{22}	0.3753	0.3738	0.3735	2.30	0.3734	0.3736	0.3740
\mathcal{T}_h^7	ω_{11}	0.1180	0.1169	0.1167	1.90	0.1166	0.1166	0.1171
	ω_{21}	0.1974	0.1954	0.1950	2.15	0.1948	0.1949	0.1951
	ω_{12}	0.3151	0.3095	0.3082	2.08	0.3078	0.3083	0.3093
	ω_{22}	0.3772	0.3743	0.3736	2.22	0.3734	0.3736	0.3740

It can be seen from Tables 6 and 7 that our method converges with a quadratic order.

4.3 Buckling of plates

The effectiveness of the MDF method for buckling analysis are demonstrated by examples with different thickness, boundary conditions and different in-plane compressive stress σ .

We have computed approximations of the buckling coefficients $\lambda^{bc} = \lambda^{bp}t^2$ being the smallest (the critical load) by which the chosen in-plane compressive stress σ must be multiplied by in order to cause buckling. In order to compare our results with those in [33, 34, 42], a non-dimensional buckling intensity is defined as:

$$K := \frac{\lambda_h^{bc} L}{\pi^2 D},$$

here $\lambda_h^{bc} = \lambda_h^{bp}t^2$ are the computed buckling coefficients, L is the plate side length and D is the flexural rigidity defined as $D = Et^3/[12(1 - \nu^2)]$.

4.3.1 Uniformly compressed plate

In this couple of tests, we use $\sigma = \mathbf{I}$, corresponding to a uniformly compressed plate (in the x, y directions).

First, we consider a simply supported plate, since analytical solutions are available (see [45]) for that case. In Table 8, we report the four lowest non-dimensional buckling intensities K_1, \dots, K_4 , for the thickness $t = 0.01$, and $L = 1$ computed by Method 3 with four different family of meshes. The table includes computed orders of convergence, as well as more accurate values extrapolated by means of a least-squares procedure. Furthermore, the last column reports the exact buckling intensities. In this case, we have used a Poisson ratio $\nu = 0.3$ and a correction factor $k = 5/6$.

Table 8 Lowest non-dimensional buckling intensities K_1, \dots, K_4 for a SSSS square plate and $t = 0.01$

Mesh	K	$N = 16$	$N = 32$	$N = 64$	Order	Extrap.	Exact
\mathcal{T}_h^3	K_1	2.0315	2.0075	2.0011	1.90	1.9987	1.9989
	K_2	5.1607	5.0381	5.0046	1.87	4.9920	4.9930
	K_3	5.2262	5.0541	5.0086	1.92	4.9922	4.9930
	K_4	8.5170	8.1249	8.0186	1.88	7.9788	7.9820
\mathcal{T}_h^4	K_1	2.0381	2.0086	2.0013	2.01	1.9989	1.9989
	K_2	5.2116	5.0465	5.0063	2.04	4.9934	4.9930
	K_3	5.2116	5.0465	5.0063	2.04	4.9934	4.9930
	K_4	8.6292	8.1388	8.0209	2.06	7.9839	7.9820
\mathcal{T}_h^5	K_1	2.0412	2.0093	2.0015	2.02	1.9989	1.9989
	K_2	5.2242	5.0485	5.0063	2.06	4.9931	4.9930
	K_3	5.2929	5.0641	5.0099	2.08	4.9932	4.9930
	K_4	8.6788	8.1504	8.0234	2.06	7.9836	7.9820
\mathcal{T}_h^7	K_1	2.0347	2.0068	2.0010	2.27	1.9995	1.9989
	K_2	5.1962	5.0424	5.0053	2.05	4.9935	4.9930
	K_3	5.2429	5.0451	5.0063	2.35	4.9968	4.9930
	K_4	8.5851	8.1192	8.0158	2.17	7.9862	7.9820

It can be seen from Table 8 that our method converges to the exact values with a quadratic order.

As a second test, we present the results for the lowest non-dimensional buckling intensity K_1 for a clamped plate with varying thickness t , in order to assess the stability of the Method 3 when t goes to zero. It is well known that K_1 converges to the non-dimensional buckling intensity of an identical Kirchhoff-Love uniformly compressed clamped plate.

In Table 9, we report the lowest non-dimensional buckling intensity K_1 of a uniformly compressed clamped plate with varying thickness t and $L = 1$. We have used five different family of meshes. The table includes computed orders of convergence, as well as more accurate values extrapolated by means of a least-squares procedure. In the last row of each family of meshes we report the limit values as t goes to zero obtained by extrapolation. In this case, we have used a Poisson ratio $\nu = 0.25$ and a correction factor $k = 5/6$.

Table 9 Lowest non-dimensional buckling intensity K_1 of a clamped plate with varying thickness.

Mesh	t	$N = 16$	$N = 32$	$N = 64$	Order	Extrap.
\mathcal{T}_h^1	0.1	4.9031	4.6658	4.6099	2.09	4.5929
	0.01	7.1314	5.5307	5.3275	2.98	5.2982
	0.001	9.9817e+1	9.2546	5.6315	4.00	4.3035
	0.0001	9.2723e+3	2.6878e+2	1.2923e+1	4.00	-0.1678
	0 (extrap.)	—	—	—	—	—
\mathcal{T}_h^2	0.1	4.6316	4.6015	4.5937	1.93	4.5909
	0.01	5.3423	5.3072	5.2981	1.96	5.2950
	0.001	5.3509	5.3157	5.3066	1.96	5.3035
	0.0001	5.3510	5.3158	5.3067	1.96	5.3035
	0 (extrap.)	5.3510	5.3158	5.3067	1.96	5.3036
\mathcal{T}_h^3	0.1	4.6476	4.6058	4.5948	1.92	4.5908
	0.01	5.3611	5.3121	5.2994	1.94	5.2949
	0.001	5.3697	5.3207	5.3079	1.94	5.3034
	0.0001	5.3698	5.3208	5.3080	1.94	5.3035
	0 (extrap.)	5.3698	5.3208	5.3080	1.94	5.3035
\mathcal{T}_h^4	0.1	4.6441	4.6043	4.5943	2.00	4.5910
	0.01	5.3564	5.3103	5.2989	2.01	5.2951
	0.001	5.3649	5.3188	5.3074	2.01	5.3036
	0.0001	5.3649	5.3189	5.3074	2.01	5.3037
	0 (extrap.)	5.3650	5.3189	5.3074	2.01	5.3037
\mathcal{T}_h^5	0.1	4.6487	4.6054	4.5946	2.00	4.5909
	0.01	5.3702	5.3128	5.2993	2.09	5.2952
	0.001	5.3863	5.3240	5.3085	2.01	5.3034
	0.0001	5.3866	5.3242	5.3088	2.01	5.3036
	0 (extrap.)	5.3867	5.3242	5.3087	2.01	5.3036

Additionally, we have also computed the lowest buckling intensity of a Kirchhoff-Love plate by using the finite element method analyzed in [41].

In Table 10, we report the lowest non-dimensional buckling intensity of a uniformly compressed clamped plate with $L = 1$. In this case we considered a Poisson ratio $\nu = 0.25$.

Table 10 Lowest non-dimensional buckling intensity of a uniformly compressed clamped thin plate (Kirchhoff-Love model) computed with the method from [41].

Method	$N = 24$	$N = 36$	$N = 48$	$N = 60$	Order	Extrapolated
[41]	5.3051	5.3042	5.3039	5.3038	2.61	5.3037

It is clear from the results of Tables 9 and 10, that our Method 3 lead to wrong result for triangular meshes \mathcal{T}_h^1 when the thickness of the plate is small, see Remark 3. For all the other family of meshes the method is locking free and do not deteriorate as the plate thickness become smaller.

4.3.2 Plate uniformly compressed in one direction

In this couple of tests, we use

$$\boldsymbol{\sigma} = \begin{bmatrix} 1 & 0 \\ 0 & 0 \end{bmatrix},$$

corresponding to a plate subjected to uniaxial compression (in the x direction). We consider different boundary conditions.

In Tables 11 and 12, we report the lowest non-dimensional buckling intensity K_1 , for a clamped and simply supported plate, respectively, with thickness $t = 0.1$, and $L = 1$ computed by Method 3 with different family of meshes. The table includes computed orders of convergence, as well as more accurate values extrapolated by means of a least-squares procedure. Furthermore, the last two columns show the results reported in [33, 34]. In these cases, we have used a Poisson ratio $\nu = 0.3$ and a correction factor $k = 5/6$.

Table 11 Lowest non-dimensional buckling intensity K_1 for a CCCC square plate and $t = 0.1$

Mesh	K	$N = 32$	$N = 64$	$N = 128$	Order	Extrap.	[33]	[34]
\mathcal{T}_b^2	K_1	8.3849	8.3157	8.2978	1.95	8.2915	8.2917	8.2931
\mathcal{T}_b^3	K_1	8.4222	8.3260	8.3004	1.91	8.2912	8.2917	8.2931
\mathcal{T}_b^4	K_1	8.3987	8.3185	8.2984	2.00	8.2917	8.2917	8.2931
\mathcal{T}_b^5	K_1	8.4273	8.3255	8.3001	2.00	8.2916	8.2917	8.2931
\mathcal{T}_b^6	K_1	8.3663	8.3110	8.2963	1.91	8.2910	8.2917	8.2931
\mathcal{T}_b^7	K_1	8.3715	8.3121	8.2965	1.93	8.2909	8.2917	8.2931

Table 12 Lowest non-dimensional buckling intensity K_1 for a SSSS square plate and $t = 0.1$

Mesh	K	$N = 32$	$N = 64$	$N = 128$	Order	Extrap.	[33]	[34]
\mathcal{T}_b^2	K_1	3.7993	3.7897	3.7873	1.97	3.7864	3.7865	3.7873
\mathcal{T}_b^3	K_1	3.8029	3.7907	3.7875	1.96	3.7864	3.7865	3.7873
\mathcal{T}_b^4	K_1	3.8049	3.7911	3.7876	2.00	3.7864	3.7865	3.7873
\mathcal{T}_b^5	K_1	3.8062	3.7913	3.7877	2.01	3.7865	3.7865	3.7873
\mathcal{T}_b^6	K_1	3.7975	3.7892	3.7871	1.98	3.7864	3.7865	3.7873
\mathcal{T}_b^7	K_1	3.8011	3.7903	3.7874	1.90	3.7863	3.7865	3.7873

It can be seen from Tables 11 and 12 that our method converges with a quadratic order.

4.3.3 Shear loaded plate

In this test, we use

$$\boldsymbol{\sigma} = \begin{bmatrix} 0 & 1 \\ 1 & 0 \end{bmatrix},$$

corresponding to a plate subjected to shear load. We consider different boundary conditions.

In Table 13, we report the lowest non-dimensional buckling intensity K_1 , for a simply supported plate with thickness $t = 0.01$, and $L = 1$ computed by Method 3 with different family of meshes. The table includes computed orders of convergence, as well as more accurate values extrapolated by means of a least-squares procedure. Furthermore, the last two columns show the results reported in [42]. In these cases, we have used a Poisson ratio $\nu = 0.3$ and a correction factor $k = 5/6$.

Table 13 Lowest non-dimensional buckling intensity K_1 for a SSSS square plate and $t = 0.01$

Mesh	K	$N = 32$	$N = 64$	$N = 128$	Order	Extrap.	[42]
\mathcal{T}_h^2	K_1	9.4832	9.3514	9.3180	1.98	9.3067	9.2830
\mathcal{T}_h^3	K_1	9.3848	9.3270	9.3119	1.94	9.3066	9.2830
\mathcal{T}_h^4	K_1	9.4602	9.3450	9.3164	2.01	9.3069	9.2830
\mathcal{T}_h^5	K_1	9.4759	9.3483	9.3170	2.03	9.3069	9.2830
\mathcal{T}_h^6	K_1	9.4196	9.3346	9.3134	2.01	9.3064	9.2830
\mathcal{T}_h^r	K_1	9.4640	9.3460	9.3163	1.99	9.3063	9.2830

It can be seen from Table 13 that our method converges with a quadratic order.

5 Conclusions

We assessed numerically the actual performance of the method proposed in [11], extending it also to free vibration and buckling problems of plates. We tested different families of mimetic meshes, different values of the relative thickness and various boundary conditions. In all the three types of problems considered (source problem, free vibration, buckling) the method was shown to be locking free and to converge with an optimal rate both in discrete L^∞ and H^1 norms for meshes made with elements with 4 or more edges. In some occasions, a super convergence rate was noticed. Moreover, differently from standard quadrilateral finite elements, the method shows a robust behavior also for uniformly distorted families of meshes such as those in Figure 5. We thus conclude that the proposed method is very reliable for Reissner-Mindlin plate computations.

Acknowledgements The third author was partially supported by CONICYT-Chile through FONDECYT project No. 11100180, and by Centro de Investigación en Ingeniería Matemática (CI²MA), Universidad de Concepción, Chile.

References

1. D. N. ARNOLD AND R. S. FALK, A uniformly accurate finite element method for the Reissner-Mindlin plate. *SIAM J. Numer. Anal.*, **26** (1989) 1276–1290.
2. F. AURICCHIO AND C. LOVADINA, Analysis of kinematic linked interpolation methods for Reissner-Mindlin plate problems. *Comput. Methods Appl. Mech. Engrg.*, **190** (2001) 2465–2482.
3. K. J. BATHE AND E. N. DVORKIN, A four-node plate bending element based on Mindlin-Reissner plate theory and a mixed interpolation. *Int. J. Numer. Methods Engrg.*, **21** (1985) 367–383.
4. L. BEIRÃO DA VEIGA, Finite element methods for a modified Reissner-Mindlin free plate model. *SIAM J. Numer. Anal.*, **42** (2004) 1572–1591.

5. L. BEIRÃO DA VEIGA, A mimetic discretization method for linear elasticity. *M2AN Math. Model. Numer. Anal.*, **44** (2010) 231–250.
6. L. BEIRÃO DA VEIGA, V. GYRYA, K. LIPNIKOV AND G. MANZINI, Mimetic finite difference method for the Stokes problem on polygonal meshes. *J. Comput. Phys.*, **228** (2009) 7215–7232.
7. L. BEIRÃO DA VEIGA AND K. LIPNIKOV, A mimetic discretization of the Stokes problem with selected edge bubbles. *SIAM J. Sci. Comput.*, **32** (2010) 875–893.
8. L. BEIRÃO DA VEIGA, K. LIPNIKOV AND G. MANZINI, Convergence analysis of the high-order mimetic finite difference method. *Numer. Math.*, **113** (2009) 325–356.
9. L. BEIRÃO DA VEIGA, K. LIPNIKOV AND G. MANZINI, Arbitrary-order nodal mimetic discretizations of elliptic problems on polygonal meshes. *SIAM J. Numer. Anal.*, **49** (2011) 1737–1760.
10. L. BEIRÃO DA VEIGA AND G. MANZINI, An a posteriori error estimator for the mimetic finite difference approximation of elliptic problems. *Int. J. Numer. Methods Engrg.*, **76** (2008) 1696–1723.
11. L. BEIRÃO DA VEIGA AND D. MORA, A mimetic discretization of the Reissner-Mindlin plate bending problem. *Numer. Math.*, **117** (2011) 425–462.
12. M. BERNDT, K. LIPNIKOV, J. D. MOULTON AND M. SHASHKOV, Convergence of mimetic finite difference discretizations of the diffusion equation. *East-West J. Numer. Math.*, **9** (2001) 253–284.
13. M. BERNDT, K. LIPNIKOV, M. SHASHKOV, M. WHEELER AND I. YOTOV, Superconvergence of the velocity in mimetic finite difference methods on quadrilaterals. *SIAM J. Numer. Anal.*, **43** (2005) 1728–1749.
14. F. BREZZI, K. J. BATHE AND M. FORTIN, Mixed-interpolated elements for Reissner-Mindlin plates. *Int. J. Numer. Methods Engrg.*, **28** (1989) 1787–1801.
15. F. BREZZI, A. BUFFA AND K. LIPNIKOV, Mimetic finite differences for elliptic problems. *M2AN Math. Model. Numer. Anal.*, **43** (2009) 277–295.
16. F. BREZZI AND M. FORTIN, *Mixed and Hybrid Finite Element Methods*. Springer-Verlag, New York, 1991.
17. F. BREZZI, M. FORTIN AND R. STENBERG, Error analysis of mixed-interpolated elements for Reissner-Mindlin plates. *Math. Models Methods Appl. Sci.*, **1** (1991) 125–151.
18. F. BREZZI, K. LIPNIKOV AND M. SHASHKOV, Convergence of the mimetic finite difference method for diffusion problems on polyhedral meshes. *SIAM J. Numer. Anal.*, **43** (2005) 1872–1896.
19. F. BREZZI, K. LIPNIKOV, M. SHASHKOV AND V. SIMONCINI, A new discretization methodology for diffusion problems on generalized polyhedral meshes *Comput. Methods Appl. Mech. Engrg.*, **196** (2007) 3682–3692.
20. F. BREZZI, K. LIPNIKOV AND V. SIMONCINI, A family of mimetic finite difference methods on polygonal and polyhedral meshes. *Math. Models Methods Appl. Sci.*, **15** (2005) 1533–1551.
21. J. CABELL AND M. SHASHKOV, A tensor artificial viscosity using a mimetic finite difference algorithm *J. Comput. Phys.*, **172** (2001) 739–765.
22. A. CANGIANI AND G. MANZINI, Flux reconstruction and pressure post-processing in mimetic finite difference methods *Comput. Methods Appl. Mech. Engrg.*, **197** (2008) 933–945.
23. A. CANGIANI, G. MANZINI AND A. RUSSO, Convergence Analysis of the mimetic finite difference method for elliptic problems *SIAM J. Numer. Anal.*, **47** (2009) 2612–2637.
24. C. CHINOSI, C. LOVADINA AND L. D. MARINI, Nonconforming locking-free finite elements for Reissner-Mindlin plates. *Comput. Methods Appl. Mech. Engrg.*, **195** (2006) 3448–3460.
25. D. J. DAWE AND O. L. ROUFAEIL, Rayleigh-Ritz vibration analysis of Mindlin plates. *J. Sound. Vib.*, **12** (1980) 345–359.
26. J. DRONIOU, R. EYMARD, T. GALLOUET AND R. HERBIN, A unified approach to mimetic finite difference, hybrid finite volume and mixed finite volume method. *Math. Models Methods Appl. Sci.*, **20** (2010) 265–295.
27. R. DURÁN, E. HERNÁNDEZ, E. LIBERMAN, R. RODRÍGUEZ AND J. SOLOMIN, Error estimates for low-order isoparametric quadrilateral finite elements for plates. *SIAM J. Numer. Anal.*, **41** (2003) 1751–1772.
28. R. DURÁN, L. HERVELLA-NIETO, E. LIBERMAN, R. RODRÍGUEZ AND J. SOLOMIN, Approximation of the vibration modes of a plate by Reissner-Mindlin equations. *Math. Comp.*, **68** (1999) 1447–1463.

29. R. DURÁN AND E. LIBERMAN, On mixed finite elements methods for the Reissner-Mindlin plate model. *Math. Comp.*, **58** (1992) 561–573.
30. H. C. HUANG AND E. HINTON, A nine node Lagrangian Mindlin plate element with enhanced shear interpolation. *Eng. Comput.*, **1** (1984) 369–379.
31. J. HYMAN, J. MOREL, M. SHASHKOV AND S. STEINBERG, Mimetic finite difference methods for diffusion equations. *Comput. Geosci.*, **6** (2002) 333–352.
32. J. HYMAN, M. SHASHKOV AND S. STEINBERG, The numerical solution of diffusion problems in strongly heterogeneous non-isotropic materials *J. Comput. Phys.*, **132** (1997) 130–148.
33. S. KITIPORNCHAI, Y. XIANG, C.M. WANG AND K.M. LIEW, Buckling of thick skew plates. *Int. J. Numer. Methods Engrg.*, **36** (1993) 1299–1310.
34. K.M. LIEW AND X.L. CHEN, Buckling of rectangular Mindlin plates subjected to partial in-plane edge loads using the radial point interpolation method. *Int. J. Solids Struct.*, **41** (2004) 1677–1695.
35. K. LIPNIKOV, G. MANZINI, F. BREZZI AND A. BUFFA, The mimetic finite difference method for the 3D magnetostatic field problems on polyhedral meshes. *J. Comput. Phys.*, **230** (2011) 305–328.
36. K. LIPNIKOV, M. SHASHKOV AND I. YOTOV, Local flux mimetic finite difference methods. *Numer. Math.*, **112** (2009) 115–152.
37. C. LOVADINA, Analysis of a mixed finite element method for the Reissner-Mindlin plate problems. *Comput. Methods Appl. Mech. Engrg.*, **163** (1998) 71–85.
38. C. LOVADINA, A low-order nonconforming finite element for Reissner-Mindlin plates. *SIAM J. Numer. Anal.*, **42** (2005) 2688–2705.
39. C. LOVADINA, D. MORA AND R. RODRÍGUEZ, Approximation of the buckling problem for Reissner-Mindlin plates. *SIAM J. Numer. Anal.*, **48** (2010) 603–632.
40. M. LYLÝ, J. NIIRANEN AND R. STENBERG, A refined error analysis of MITC plate elements. *Math. Models Methods Appl. Sci.*, **16** (2006) 967–977.
41. D. MORA AND R. RODRÍGUEZ, A piecewise linear finite element method for the buckling and the vibration problems of thin plates. *Math. Comp.*, **78** (2009) 1891–1917.
42. H. NGUYEN-XUAN, G.R. LIU, C. THAI-HOANG AND T. NGUYEN-THOI, An edge-based smoothed finite element method (ES-FEM) with stabilized discrete shear gap technique for analysis of Reissner-Mindlin plates. *Comput. Methods Appl. Mech. Engrg.*, **199** (2010) 471–489.
43. P. PEISKER AND D. BRAESS, Uniform convergence of mixed interpolated elements for Reissner-Mindlin plates. *M2AN Math. Model. Numer. Anal.*, **26** (1992) 557–574.
44. J. PITKÄRANTA AND M. SURI, Design principles and error analysis for reduced-shear plate-bending finite elements. *Numer. Math.*, **75** (1996) 223–266.
45. J. N. REDDY, *Mechanics of Laminated Composite Plates - Theory and Analysis*. CRC Press, Boca Raton, 1997.